

DISSOCIATION, FRAGMENTATION AND FISSION OF SIMPLE METAL CLUSTERS*

CONSTANTINE YANNOULEAS, UZI LANDMAN AND ROBERT N. BARNETT

*School of Physics, Georgia Institute of Technology
Atlanta, Georgia 30332-0430*

I. INTRODUCTION

Dissociation, fragmentation, and fissioning processes underly physical and chemical phenomena in a variety of finite-size systems, characterized by a wide spectrum of energy scales, nature of interactions, and characteristic spatial and temporal scales. These include nuclear fission [1,2], unimolecular decay and reactions in atoms and molecules [3], and more recently dissociation and fragmentation processes in atomic and molecular clusters [4–6]. Investigations of the energetics, mechanisms, pathways, and dynamics of fragmentation processes provide ways and means for explorations of the structure, stability, excitations, and dynamics in the many-body finite systems mentioned above, as well as they allow for comprehensive tests of theoretical methodologies and conceptual developments, and have formed active areas of fruitful research endeavors in nuclear physics, and more recently in cluster science.

Under the general title of dissociation and fragmentation [7] processes in metal clusters, one usually distinguishes two classes of phenomena, i.e., (1) dissociation of neutral monomers and/or dimers, and (2) fission. The physical processes in the first class are most often referred to as evaporation of monomers and/or dimers, since they are endothermic processes and are usually induced through laser heating of the cluster. The unimolecular equations associated with these processes are

$$M_N^+ \longrightarrow M_{N-1}^+ + M , \quad (1)$$

for monomer separation, and

$$M_N^+ \longrightarrow M_{N-2}^+ + M_2 , \quad (2)$$

for dimer separation (N denotes the number of atoms in the clusters [8]). The parent clusters M_N^+ have been taken here as being singly ionized, in order to conform with available experimental measurements [4]. Fission on the other hand, is most often an exothermic process and is due to the Coulombic forces associated with excess charges on the cluster. It

* Contributed Chapter to the book **Metal Clusters**, Edited by W. Ekardt (Wiley, New York, 1999) pp. 145-180.

has been found that the minimum excess charge required to induce fission is 2 elementary units (either positive or negative). In this case the doubly-charged parent cluster splits into two singly charged fragments, and the corresponding unimolecular equation can be written as

$$M_N^{2\pm} \longrightarrow M_P^{1\pm} + M_{N-P}^{1\pm}, \quad P = 1, \dots, [N/2]. \quad (3)$$

It needs to be emphasized that fragmentation through fission involves most often the overcoming of a fission barrier, while monomer and dimer separation are barrierless processes [4].

A. Metal cluster fission and nuclear fission: Similarities and differences

Multiply charged metallic clusters (M_N^{Z+}) are observable in mass spectra if they exceed a critical size of stability N_c^{Z+} (e.g. for $Z = 2$, $N_c^{2+} = 27$ for Na and $N_c^{2+} = 20$ for K [4,9]). For clusters with $N > N_c^{Z+}$, evaporation of neutral species is the preferred dissociation channel, while, below the critical size, fission into two charged fragments dominates (for $Z = 2$, two singly charged fragments emerge). Nevertheless, at low enough temperature, such M_N^{Z+} ($N < N_c^{Z+}$) clusters can be metastable above a certain size N_b^{Z+} , because of the existence of a fission barrier E_b (for Na_N^{2+} and K_N^{2+} , $N_b^{2+} = 7$ [10,11]).

These observations indicate that fission of metal clusters occurs when the repulsive Coulomb forces due to the accumulation of the excess charges overcome the electronic binding (cohesion) of the cluster. This reminds us immediately of the well-studied nuclear fission phenomenon and the celebrated Liquid Drop Model (LDM) according to which the binding nuclear forces are expressed as a sum of volume and surface terms, and the balance between the Coulomb repulsion and the increase in surface area upon volume conserving deformations allows for an estimate of the stability and fissility of the nucleus [12,13].

We note that for doubly charged metal clusters with $N \leq 12$ microscopic descriptions of energetics and dynamics of fission, based on first-principles electronic-structure calculations in conjunction with molecular dynamics (MD) simulations, have been performed [10,11] (see section III.C.1 for details). Several of the trends exhibited by the microscopic calculations (such as influence of magic numbers, associated with electronic shell closing, on fission energetics and barrier heights; predominance of an asymmetric fission channel; double-humped fission-barrier shapes; shapes of deforming clusters along the fission trajectory portraying two fragments connected through a stretching neck) suggest that appropriate adaptation of methodologies developed originally in the context of nuclear fission may provide a useful conceptual and calculational framework for studies of systematics and patterns of fission processes in metallic clusters.

In this context, it is useful to comment on the earliest treatments of pertinent nuclear processes, i.e., fission [12,1] and alpha radioactivity [14,15,2]. Adaptation of the simple one-center LDM to charged metallic clusters [5], involving calculation of the Coulomb repulsive energy due to an excess charge localized at the surface, yields a reduced LDM fissility parameter $\xi = (Z^2/N)/(Z^2/N)_{cr}$, where $(Z^2/N)_{cr} = 16\pi r_s^3 \sigma / e^2$ with the surface energy per unit area denoted by σ and r_s being the Wigner-Seitz radius (using bulk r_s and σ values, $(Z^2/N)_{cr} = 0.44$ and 0.39 for K_N^{Z+} and Na_N^{Z+} , respectively). Accordingly, a cluster

is unstable for $\xi > 1$ (implying that for K_N^{2+} with $N \leq 9$ and Na_N^{2+} with $N \leq 10$ barrierless fission should occur) with the most favorable channel being the symmetric one (i.e., when the two fragments have equal masses, which is only approximately true for nuclear fission, and certainly not the case for small metal clusters). For $0.351 < \xi < 1$, the system is metastable (i.e., may fission in a process involving a barrier), and for $0 < \xi < 0.351$ the system is stable.

At the other limit, α -radioactivity, which may be viewed as an extreme case of (super)asymmetric fission, is commonly described as a process where the fragments are formed (or as often said, preformed) before the system reaches the top of the barrier (saddle point), and as a result the barrier is mainly Coulombic [2]. We note here that asymmetric emission of heavier nuclei is also known (e.g., $^{223}\text{Ra} \rightarrow ^{14}\text{C} + ^{209}\text{Pb}$, referred to as exotic or cluster radioactivity [16–18]), and the barriers in these cases resemble the one-humped barrier of alpha radioactivity and do not exhibit modulations due to shell effects [18]. We also remark that such α -radioactivity-type (essentially Coulombic) barriers have been proposed recently [19] for describing the overall shape of the fission barriers in the case of metal clusters.

Although, several aspects of the simple LDM (e.g., competition between Coulomb and surface terms) and the α -particle, Coulombic model (e.g., asymmetric channels and a scission configuration close to the location of the saddle of the multi-dimensional potential-energy surface) are present in the fission of metal clusters, neither model is adequate in light of the characteristic behavior revealed from the microscopic calculations and experiments. Rather, we find that proper treatments of fission in these systems require consideration of shell effects (for a recent experimental study that demonstrates the importance of shell effects in metal-cluster fission, see Ref. [9b]). While such effects are known to have important consequences in nuclear fission (transforming the one-humped LDM barrier for symmetric fission into a two-humped barrier [20,2]), their role in the case of metal clusters goes even further. Indeed, as illustrated below (see section III.C.2) for the case of the magic Na_{10}^{2+} (8 delocalized electrons), shell effects can be the largest contribution to the fission barrier, in particular in instances when the LDM component exhibits no barrier (in this case the LDM fissility $\xi > 1$). In this respect, Na_{10}^{2+} is analogous to the case of superheavy nuclei, which are believed [21] to be stabilized by the shell structure of a major shell closure at $Z_p = 114$, $N_n = 184$ (Z_p is the number of protons and N_n is the number of neutrons; unfortunately such nuclei have not been yet observed or synthesized artificially).

B. Other decay modes in atomic and molecular clusters

In this chapter, we will concentrate on the unimolecular processes in metal clusters described by Eqs. (1–3). However, there is a variety of additional dissociation and fragmentation modes in atomic and molecular clusters (see reviews in Ref. [22]), which have been discovered experimentally or anticipated theoretically; among them we mention:

1. Unimolecular fission of triply and higher charged cationic simple metal clusters [6,23,24];
2. Metastability against electron autodetachment of multiply charged *anionic* atomic clusters [25–27] and fullerenes [26–28];

3. Fragmentation of cationic fullerenes via sequential evaporation of carbon dimers [29];
4. Ultrarapid fragmentation of rare-gas clusters following excitation (involving excimer formation [30]) or ionization [22];
5. Multifragmentation phase transitions according to microcanonical thermodynamics of highly excited atomic clusters [31]; and
6. Pathways and dynamics of dissociation and fragmentation of ionized Van-der-Waals and hydrogen-bonded molecular clusters [22,32].

C. Organization of the chapter

In the following, we will present jellium-related theoretical approaches [specifically the Shell Correction Method (SCM) and variants thereof] appropriate for describing shell effects, energetics and decay pathways of metal-cluster fragmentation processes (both the monomer/dimer dissociation and fission), which were inspired by the many similarities with the physics of shell effects in atomic nuclei (section II). In section III, we will compare the experimental trends with the resulting theoretical SCM interpretations, and in addition we will discuss theoretical results from first-principles MD simulations (section III.C.1). Section IV will discuss some latest insights concerning the importance of electronic-entropy and finite-temperature effects. Finally, section V will provide a summary.

II. THEORY OF SHAPE DEFORMATIONS

In early applications of the jellium model, the shape of metal clusters was assumed in all instances to be spherical [33,34], but soon it became apparent that the spherical symmetry was too restrictive [35,36]. Indeed clusters with open electronic shells (between the magic numbers $N_e = 2, 8, 20, 40, 58, 92$, etc...) are subjected to Jahn-Teller distortions [37]. By now it has been well established that a quantitative description of the underlying shell effects and of fragmentation phenomena (as well as of other less complicated phenomena such as Ionization and Vertical Electron Detachment) requires a proper description of the deformed shapes of both parent and daughter clusters (of both precursor and final ionic or neutral product in the case of ionization and vertical electron detachment).

A most successful method for describing both deformation and shell effects in simple metal clusters (i.e., those that can be described by the jellium background model) is the SCM, originally developed in the field of nuclear physics [38,2]. In a series of recent publications [25,26,28,39–45], the SCM was further developed, adapted, and applied in the realm of finite-size, condensed-matter nanostructures (i.e., metal clusters [25,26,39–43], but also multiply charged fullerenes [28], ^3He clusters [44], and metallic nanowires and nanoconstrictions [45]). Additionally, Refs. [46–49] have used semiempirical versions (see below) of the SCM to study the shapes of neutral Na clusters [46,47] and aspects of metal-cluster fission [48,49].

The SCM derives its justification from the local-density-approximation (LDA) functional theory and has been developed as a two-level method.

At the microscopic level, referred to as the LDA-SCM, the method has been shown to be a non-selfconsistent approximation to the Kohn-Sham (KS) –LDA approach [50]. Apart from computational efficiency, an important physical insight provided by the LDA-SCM is that the total KS-LDA energy $E_{\text{total}}(N)$ [or in another notation $E_{\text{KS}}(N)$] of a finite system of interacting delocalized electrons (or more generally of other fermions, like nucleons or ^3He atoms) can be divided into two contributions, i.e.,

$$E_{\text{total}}(N) = \tilde{E}(N) + \Delta E_{\text{sh}}(N) , \quad (4)$$

where \tilde{E} is the part that varies smoothly as a function of the system size (e.g., the number, N of atoms in a metal cluster), while $\Delta E_{\text{sh}}(N)$ is an oscillatory term accounting for the shell effects; it arises from the discretization of the electronic states (quantum size effect). $\Delta E_{\text{sh}}(N)$ is usually called a shell correction in the nuclear [38,1] and cluster [25,26] literature.

Starting from the fundamental microscopic separation in Eq. (4), various semiempirical implementations (referred to as SE-SCM, see section II.B) of such a division consist of different approximate choices and methods for evaluating the two terms contributing to this separation.

As an illustration of the physical content of Eq. (4) (which as well serves as a motivating example for the SCM), we show in Fig. 1 the size-evolutionary pattern of the Ionization Potentials (IPs) of Na_N clusters, which exhibits odd-even oscillations in the observed spectrum in addition to the major features (major IP drops) at the magic numbers. Theoretical calculations at three different levels are contrasted to the experimental observations, namely, a smooth description of the pattern [Inset (a)], and two levels of shell-corrected descriptions — one assuming spherical symmetry [Inset (b)], and the other allowing for triaxial shape deformations [Fig. 1, main frame]. The progressive improvement of the level of agreement between the experimental [51,52] and theoretical patterns is evident.

Below, we first outline the microscopic derivation of Eq. (4), and subsequently we proceed with a presentation of the SE-SCM.

A. Microscopic Foundation of Shell Correction Methods – The LDA-SCM

The LDA-SCM approach, which has been shown to yield results in excellent agreement with self-consistent KS-LDA calculations [25,26], is equivalent to a Harris functional [53] approximation ($E_{\text{Harris}}[\rho^{\text{in}}]$, see below) to the KS-LDA total energy [50] ($E_{\text{KS}}[\rho_{\text{KS}}]$), with the input density ρ^{in} obtained through a variational minimization of an extended Thomas-Fermi (ETF) energy functional, $E_{\text{ETF}}[\rho]$.

The property of the non-selfconsistent Harris functional to yield total energies close to the KS-LDA ones is based on the following equality:

$$E_{\text{KS}}[\rho_{\text{KS}}] = E_{\text{Harris}}[\rho^{\text{in}}] + O(\delta\rho^2) , \quad (5)$$

where $\delta\rho = \rho_{\text{KS}} - \rho^{\text{in}}$. Namely, the KS-LDA energy is, to second-order in $\delta\rho$, equal to the Harris energy.

Several recent publications have proven [54–56] the validity of equation (5) in connection with the Harris functional, which is often used in electronic structure calculations of

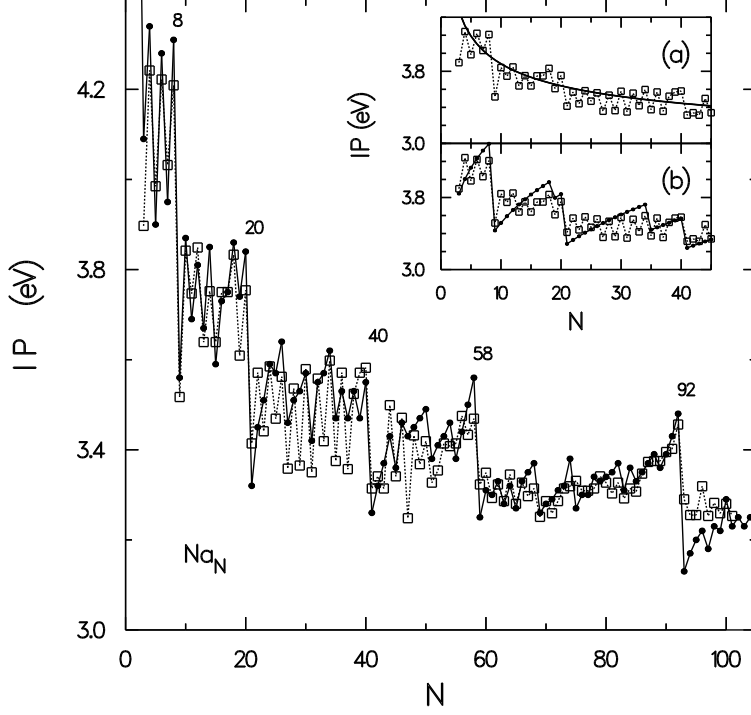


FIG. 1. IPs of Na_N clusters. Open squares: Experimental measurements [51,52]. Solid circles: Theoretical IPs derived from the SCM assuming ellipsoidal (triaxial) deformations. Inset (a): The solid line represents the smooth contribution to the theoretical SCM IPs. Inset (b): The solid circles are the IPs derived from the SCM assuming spherical symmetry.

molecules, surfaces, and other condensed-matter systems. We note that, in the context of nuclear physics, Strutinsky had earlier proven [38] the validity of Eq. (5), with the difference that he utilized the Hartree-Fock (HF) functional instead of the KS-LDA one. In the nuclear-physics literature, the HF version of Eq. (5) is referred to as the Strutinsky theorem.

Usually, in the Harris functional, the *input* density ρ^{in} is taken as a superposition of site densities. Initially [53], the site components of the input density were not optimized. Later [55,56], it was realized that the results could be improved by variationally adjusting the site components through a *maximization* of the Harris functional itself. However, doing so adds the burden of a matrix diagonalization for obtaining the eigenvalues (see below) at each step of the variation. Our method differs from the Harris approach in that the optimization of the input density is achieved by us through a variational ETF method [57] (which does not require such a step-by-step matrix diagonalization).

The non-selfconsistent Harris functional is given by the following expression,

$$E_{\text{Harris}}[\rho^{\text{in}}] = E_{\text{I}} + \sum_{i=1}^{\text{occ}} \epsilon_i^{\text{out}} - \int \left\{ \frac{1}{2} V_H[\rho^{\text{in}}(\mathbf{r})] + V_{\text{xc}}[\rho^{\text{in}}(\mathbf{r})] \right\} \rho^{\text{in}}(\mathbf{r}) d\mathbf{r} + \int \mathcal{E}_{\text{xc}}[\rho^{\text{in}}(\mathbf{r})] d\mathbf{r}, \quad (6)$$

where V_H is the Hartree (electronic) repulsive potential, E_{I} is the repulsive electrostatic energy of the ions, and $E_{\text{xc}}[\rho] \equiv \int \mathcal{E}_{\text{xc}}[\rho] d\mathbf{r}$ is the exchange-correlation (xc) functional [58]

[the corresponding xc potential is given as $V_{xc}(\mathbf{r}) \equiv \delta E_{xc}[\rho]/\delta\rho(\mathbf{r})$]. ϵ_i^{out} are the eigenvalues (non-selfconsistent) of the single-particle Hamiltonian,

$$\widehat{H} = -\frac{\hbar^2}{2m_e}\nabla^2 + V_{\text{in}} , \quad (7)$$

with the mean-field potential given by

$$V_{\text{in}}[\rho^{\text{in}}(\mathbf{r})] = V_H[\rho^{\text{in}}(\mathbf{r})] + V_{xc}[\rho^{\text{in}}(\mathbf{r})] + V_I(\mathbf{r}) , \quad (8)$$

$V_I(\mathbf{r})$ being the attractive potential between the electrons and ions.

The ETF-LDA energy functional, $E_{\text{ETF}}[\rho]$, is obtained by replacing the kinetic energy term, $T[\rho]$, in the usual LDA functional, namely in the expression,

$$E_{\text{LDA}}[\rho] = T[\rho] + \int \left\{ \frac{1}{2} V_H[\rho(\mathbf{r})] + V_I(\mathbf{r}) \right\} \rho(\mathbf{r}) d\mathbf{r} + \int \mathcal{E}_{xc}[\rho(\mathbf{r})] d\mathbf{r} + E_I , \quad (9)$$

by the ETF kinetic energy, given to the 4th-order gradients as follows [59],

$$\begin{aligned} T_{\text{ETF}}[\rho] &= \int t_{\text{ETF}}[\rho] d\mathbf{r} \\ &= \frac{\hbar^2}{2m_e} \int \left\{ \frac{3}{5} (3\pi^2)^{2/3} \rho^{5/3} + \frac{1}{36} \frac{(\nabla\rho)^2}{\rho} + \frac{1}{270} (3\pi^2)^{-2/3} \rho^{1/3} \right. \\ &\quad \times \left. \left[\frac{1}{3} \left(\frac{\nabla\rho}{\rho} \right)^4 - \frac{9}{8} \left(\frac{\nabla\rho}{\rho} \right)^2 \frac{\Delta\rho}{\rho} + \left(\frac{\Delta\rho}{\rho} \right)^2 \right] \right\} d\mathbf{r} . \end{aligned} \quad (10)$$

We would like to remind the reader that the KS kinetic energy is of course given by the expression

$$T_{\text{KS}}[\rho_{\text{KS}}] = \sum_{i=1}^{\text{occ}} \langle \phi_{\text{KS},i} | -\frac{\hbar^2}{2m_e} \nabla^2 | \phi_{\text{KS},i} \rangle , \quad (11)$$

where the single-particle wave functions $\phi_{\text{KS},i}(\mathbf{r})$ are obtained from a self-consistent solution of the KS equations.

The optimal ETF-LDA total energy is obtained by minimization of $E_{\text{ETF}}[\rho]$ with respect to the density. In our calculations, we use for the trial densities parametrized profiles $\rho(\mathbf{r}; \{\gamma_i\})$ [60,25,26] with $\{\gamma_i\}$ as variational parameters (the ETF-LDA optimal density is denoted as $\tilde{\rho}$). The single-particle eigenvalues, $\{\epsilon_i^{\text{out}}\}$, in Eq. (6) are obtained then as the solutions to the single-particle Hamiltonian of Eq. (7) with V_{in} replaced by V_{ETF} [given by Eq. (8) with $\rho^{\text{in}}(\mathbf{r})$ replaced by $\tilde{\rho}(\mathbf{r})$]. Hereafter, these single-particle eigenvalues will be denoted by $\{\tilde{\epsilon}_i\}$.

In our approach, the smooth contribution in the separation (4) of the total energy is given by $E_{\text{ETF}}[\tilde{\rho}]$, while the shell correction, ΔE_{sh} , is simply the difference [25,26]

$$\begin{aligned} \Delta E_{\text{sh}} &= E_{\text{Harris}}[\tilde{\rho}] - E_{\text{ETF}}[\tilde{\rho}] \\ &= \sum_{i=1}^{\text{occ}} \tilde{\epsilon}_i - \int \tilde{\rho}(\mathbf{r}) V_{\text{ETF}}(\mathbf{r}) d\mathbf{r} - T_{\text{ETF}}[\tilde{\rho}] . \end{aligned} \quad (12)$$

B. Semiempirical shell-correction method (SE-SCM)

1. Methodology

Rather than proceed with the microscopic route, Strutinsky proposed a method for the separation of the total energy into smooth and shell-correction terms [see Eq. (4)] based on an averaging procedure. Accordingly, a smooth part, \tilde{E}_{sp} , is extracted out of the sum of the single-particle energies $\sum_i^{\text{occ}} \tilde{\epsilon}_i$ [or $\sum_i^{\text{occ}} \epsilon_i^{\text{out}}$, see Eq. (6)] by averaging them through an appropriate procedure. Usually, but not necessarily, one replaces the delta functions in the single-particle density of states by gaussians or other appropriate weighting functions. As a result, each single-particle level is assigned an averaging occupation number \tilde{f}_i , and the smooth part \tilde{E}_{sp} is formally written as

$$\tilde{E}_{\text{sp}} = \sum_i \tilde{\epsilon}_i \tilde{f}_i . \quad (13)$$

Consequently, the Strutinsky shell correction is given by

$$\Delta E_{\text{sh}}^{\text{Str}} = \sum_{i=1}^{\text{occ}} \tilde{\epsilon}_i - \tilde{E}_{\text{sp}} . \quad (14)$$

The Strutinsky prescription (14) has the practical advantage of using only the single-particle energies $\tilde{\epsilon}_i$, and not the smooth density $\tilde{\rho}$. Taking advantage of this, the single-particle energies can be taken as those of an external potential that empirically approximates the self-consistent potential of a finite system. In the nuclear case, a modified anisotropic three-dimensional harmonic oscillator has been used successfully to describe the shell-corrections in deformed nuclei [1,2].

The single-particle smooth part, \tilde{E}_{sp} , however, is only one component in the smooth contribution $\tilde{E}[\tilde{\rho}]$, which needs to be added to the shell correction term in order to yield the total energy, i.e.,

$$E_{\text{total}} \approx \Delta E_{\text{sh}}^{\text{Str}} + \tilde{E}[\tilde{\rho}] . \quad (15)$$

Strutinsky did not address the question of how to calculate microscopically the smooth part \tilde{E} (which necessarily entails specifying the smooth density $\tilde{\rho}$). Instead he circumvented this question by substituting for \tilde{E} the empirical energies, E_{LDM} , of the nuclear liquid drop model, namely he suggested that

$$E_{\text{total}} \approx \Delta E_{\text{sh}}^{\text{Str}} + E_{\text{LDM}} . \quad (16)$$

In applications of Eq. (16), the single-particle energies involved in the averaging [see Eqs. (13) and (14)] are commonly obtained as solutions of a Schrödinger equation with phenomenological one-body potentials. This last approximation has been very successful in describing fission barriers and properties of strongly deformed nuclei using harmonic-oscillator-type or Wood-Saxon empirical potentials.

2. Liquid-drop model for neutral and charged deformed clusters

For neutral clusters, the LDM expresses [60,48,5] the *smooth* part, \tilde{E} , of the total energy as the sum of three contributions, namely a volume, a surface, and a curvature term, i.e.,

$$\begin{aligned}\tilde{E} &= E_{\text{vol}} + E_{\text{surf}} + E_{\text{curv}} \\ &= A_v \int d\tau + \sigma \int dS + A_c \int dS \kappa ,\end{aligned}\tag{17}$$

where $d\tau$ is the volume element and dS is the surface differential element. The local curvature κ is defined by the expression $\kappa = 0.5(R_{\text{max}}^{-1} + R_{\text{min}}^{-1})$, where R_{max} and R_{min} are the two principal radii of curvature at a local point on the surface of the jellium droplet (of a general shape) which models the cluster. The corresponding coefficients can be determined [25,26,60] by fitting the ETF-LDA total energy for spherical shapes (see section II.A) to the following parametrized expression as a function of the number, N , of atoms in the cluster [61],

$$E_{\text{ETF}}^{\text{sph}} = \alpha_v N + \alpha_s N^{2/3} + \alpha_c N^{1/3} .\tag{18}$$

The following expressions relate [62] the coefficients A_v , σ , and A_c to the corresponding coefficients, (α 's), in Eq. (18),

$$A_v = \frac{3}{4\pi r_s^3} \alpha_v ; \quad \sigma = \frac{1}{4\pi r_s^2} \alpha_s ; \quad A_c = \frac{1}{4\pi r_s} \alpha_c .\tag{19}$$

In the following, we will focus on the case of clusters with ellipsoidal (triaxial) shapes. In the case of ellipsoidal shapes the areal integral and the integrated curvature can be expressed in closed analytical form with the help of the incomplete elliptic integrals $\mathcal{F}(\psi, k)$ and $\mathcal{E}(\psi, k)$ of the first and second kind [63], respectively. Before writing the formulas, we need to introduce some notations. Volume conservation must be employed, namely

$$a'b'c'/R_0^3 = abc = 1 ,\tag{20}$$

where R_0 is the radius of a sphere with the same volume ($R_0 = r_s N^{1/3}$ is taken to be the radius of the positive jellium assuming spherical symmetry, r_s being the corresponding Wigner-Seitz radius), and $a = a'/R_0$, etc..., are the dimensionless semi-axes. The eccentricities are defined through the dimensionless semi-axes as follows

$$\begin{aligned}e_1^2 &= 1 - (c/a)^2 \\ e_2^2 &= 1 - (b/a)^2 \\ e_3^2 &= 1 - (c/b)^2 .\end{aligned}\tag{21}$$

The semi-axes are chosen so that

$$a \geq b \geq c .\tag{22}$$

With the notation $\sin \psi = e_1$, $k_2 = e_2/e_1$, and $k_3 = e_3/e_1$, the relative (with respect to the spherical shape) surface and curvature energies are given [64] by

$$\frac{E_{\text{surf}}^{\text{ell}}}{E_{\text{surf}}^{\text{sph}}} = \frac{ab}{2} \left[\frac{1 - e_1^2}{e_1} \mathcal{F}(\psi, k_3) + e_1 \mathcal{E}(\psi, k_3) + c^3 \right] \quad (23)$$

and

$$\frac{E_{\text{curv}}^{\text{ell}}}{E_{\text{curv}}^{\text{sph}}} = \frac{bc}{2a} \left[1 + \frac{a^3}{e_1} \left((1 - e_1^2) \mathcal{F}(\psi, k_2) + e_1^2 \mathcal{E}(\psi, k_2) \right) \right]. \quad (24)$$

The change in the smooth part of the cluster total energy due to the excess charge $\pm Z$ has been discussed for spherical clusters in Refs. [25,26]. The result may be summarized as

$$\Delta \tilde{E}^{\text{sph}}(Z) = \tilde{E}^{\text{sph}}(Z) - \tilde{E}^{\text{sph}}(0) = \mp WZ + \frac{Z(Z \pm 0.25)e^2}{2(R_0 + \delta)}, \quad (25)$$

where the upper and lower signs correspond to negatively and positively charged states, respectively, W is the work function of the metal, R_0 is the radius of the positive jellium assuming spherical symmetry, and δ is a spillout-type parameter.

To generalize the above results to an ellipsoidal shape, $\phi(R_0 + \delta) = e^2/(R_0 + \delta)$, which is the value of the potential on the surface of a spherical conductor, needs to be replaced by the corresponding expression for the potential on the surface of a conducting ellipsoid. The final result, normalized to the spherical shape, is given by the expression

$$\frac{\Delta \tilde{E}^{\text{ell}}(Z) \pm WZ}{\Delta \tilde{E}^{\text{sph}}(Z) \pm WZ} = \frac{bc}{e_1} \mathcal{F}(\psi, k_2), \quad (26)$$

where the \pm sign in front of WZ corresponds to negatively and positively charged clusters, respectively.

3. The modified Nilsson potential for ellipsoidal shapes

A natural choice for an external potential to be used for calculating shell corrections with the Strutinsky method is an anisotropic, three-dimensional oscillator with an additional \mathbf{l}^2 angular-momentum term for lifting the harmonic oscillator degeneracies [65]. Such an oscillator model for approximating the total energies of metal clusters, but without separating them into a smooth and a shell-correction part in the spirit of Strutinsky's approach, had been used [52] with some success for calculating relative energy surfaces and deformation shapes of metal clusters. However, this simple harmonic oscillator model had serious limitations, since i) the total energies were calculated by the expression $\frac{3}{4} \sum_i^{\text{occ}} \tilde{\epsilon}_i$, and thus did not compare with the total energies obtained from the KS-LDA approach, and ii) the model could not be extended to the case of charged (cationic or anionic) clusters. Thus absolute ionization potentials, electron affinities, and fission energetics could not be calculated in this model. Alternatively, in our approach, we are making only a limited use of the external oscillator potential in calculating a modified Strutinsky shell correction. Total energies are evaluated by adding this shell correction to the smooth LDM energies (which incorporate xc contributions, since the LDM coefficients are extracted via a comparison with total ETF-LDA energies, or they are taken from experimental values).

In particular, a modified Nilsson Hamiltonian appropriate for metal clusters [35,36] is given by

$$H_N = H_0 + U_0 \hbar \omega_0 (\mathbf{I}^2 - \langle \mathbf{I}^2 \rangle_n) , \quad (27)$$

where H_0 is the hamiltonian for a three-dimensional anisotropic oscillator, namely

$$\begin{aligned} H_0 &= -\frac{\hbar^2}{2m_e} \Delta + \frac{m_e}{2} (\omega_1^2 x^2 + \omega_2^2 y^2 + \omega_3^2 z^2) \\ &= \sum_{k=1}^3 (a_k^\dagger a_k + \frac{1}{2}) \hbar \omega_k . \end{aligned} \quad (28)$$

U_0 in Eq. (27) is a dimensionless parameter, which for occupied states may depend on the effective principal quantum number $n = n_1 + n_2 + n_3$ associated with the major shells of any spherical-oscillator, (n_1, n_2, n_3) being the quantum numbers specifying the single-particle levels of the hamiltonian H_0 (for clusters comprising up to 100 valence electrons, only a weak dependence on n is found, see Table I in Ref. [40a]). U_0 vanishes for values of n higher than the corresponding value of the last partially (or fully) filled major shell with reference to the spherical limit.

$\mathbf{I}^2 = \sum_{k=1}^3 l_k^2$ is a "stretched" angular momentum which scales to the ellipsoidal shape and is defined as follows,

$$l_3^2 \equiv (q_1 p_2 - q_2 p_1)^2 , \quad (29)$$

(with similarly obtained expressions for l_1 and l_2 via a cyclic permutation of indices) where the stretched position and momentum coordinates are defined via the corresponding natural coordinates, q_k^{nat} and p_k^{nat} , as follows,

$$q_k \equiv q_k^{\text{nat}} (m_e \omega_k / \hbar)^{1/2} = \frac{a_k^\dagger + a_k}{\sqrt{2}} , \quad (k = 1, 2, 3) , \quad (30)$$

$$p_k \equiv p_k^{\text{nat}} (1 / \hbar m_e \omega_k)^{1/2} = i \frac{a_k^\dagger - a_k}{\sqrt{2}} , \quad (k = 1, 2, 3) . \quad (31)$$

The stretched \mathbf{I}^2 is not a properly defined angular-momentum operator, but has the advantageous property that it does not mix deformed states which correspond to spherical major shells with different principal quantum numbers $n = n_1 + n_2 + n_3$ (see, the Appendix in Ref. [40a] for the expression of the matrix elements of \mathbf{I}^2).

The subtraction of the term $\langle \mathbf{I}^2 \rangle_n = n(n+3)/2$, where $\langle \rangle_n$ denotes the expectation value taken over the n th-major shell in spherical symmetry, guaranties that the average separation between major oscillator shells is not affected as a result of the lifting of the degeneracy.

The oscillator frequencies can be related to the principal semi-axes a' , b' , and c' [see, Eq. (20)] via the volume-conservation constraint and the requirement that the surface of the cluster is an equipotential one, namely

$$\omega_1 a' = \omega_2 b' = \omega_3 c' = \omega_0 R_0 , \quad (32)$$

where the frequency ω_0 for the spherical shape (with radius R_0) was taken according to Ref. [35] to be

$$\hbar\omega_0(N) = \frac{49 \text{ eV bohr}^2}{r_s^2 N^{1/3}} \left[1 + \frac{t}{r_s N^{1/3}} \right]^{-2} . \quad (33)$$

Since in this paper we consider solely monovalent elements, N in Eq. (33) is the number of atoms for the family of clusters $M_N^{Z\pm}$, r_s is the Wigner-Seitz radius expressed in atomic units, and t denotes the electronic spillout for the neutral cluster according to Ref. [35].

4. Shell correction and averaging of single-particle spectra for the modified Nilsson potential

Usually \tilde{E}_{sp} [see Eqs. (13) and (14)] is calculated numerically [66]. However, a variation of the numerical Strutinsky averaging method consists in using the semiclassical partition function and in expanding it in powers of \hbar^2 . With this method, for the case of an anisotropic, fully triaxial oscillator, one finds [1,67] an analytical result, namely [68]

$$\tilde{E}_{\text{sp}}^{\text{osc}} = \hbar(\omega_1\omega_2\omega_3)^{1/3} \left(\frac{1}{4}(3N_e)^{4/3} + \frac{1}{24} \frac{\omega_1^2 + \omega_2^2 + \omega_3^2}{(\omega_1\omega_2\omega_3)^{2/3}} (3N_e)^{2/3} \right) , \quad (34)$$

where N_e denotes the number of delocalized valence electrons in the cluster.

In the present work, expression (34) (as modified below) will be substituted for the average part \tilde{E}_{sp} in Eq. (14), while the sum $\sum_i^{\text{occ}} \tilde{\epsilon}_i$ will be calculated numerically by specifying the occupied single-particle states of the modified Nilsson oscillator represented by the hamiltonian (27).

In the case of an isotropic oscillator, not only the smooth contribution, $\tilde{E}_{\text{sp}}^{\text{osc}}$, but also the Strutinsky shell correction (14) can be specified analytically [1] with the result

$$\Delta E_{\text{sh},0}^{\text{Str}}(x) = \frac{1}{24} \hbar\omega_0 (3N_e)^{2/3} (-1 + 12x(1-x)) , \quad (35)$$

where x is the fractional filling of the highest partially filled harmonic-oscillator major shell. For a filled shell ($x = 0$ or 1), $\Delta E_{\text{sh},0}^{\text{Str}}(0) = -\frac{1}{24} \hbar\omega_0 (3N_e)^{2/3}$, instead of the essentially vanishing value as in the case of the ETF-LDA defined shell correction (cf. Fig. 1 of Ref. [40a]). To adjust for this discrepancy, we add $-\Delta E_{\text{sh},0}^{\text{Str}}(0)$ to $\Delta E_{\text{sh}}^{\text{Str}}$ calculated through Eq. (14) for the case of open-shell, as well as closed-shell clusters.

5. Overall procedure

We are now in a position to summarize the calculational procedure for the SE-SCM in the case of deformed clusters, which consists of the following steps:

1. Parametrize results of ETF-LDA calculations for spherical neutral jellia according to Eq. (18).

2. Use above parametrization (assuming that parameters per differential element of volume, surface, and integrated curvature are shape independent) in Eq. (17) to calculate the liquid-drop energy associated with neutral clusters, and then add to it the charging energy according to Eq. (26) to determine the total LDM energy \tilde{E} (available experimental values for σ and W can also be used).
3. Use Equations (27) and (28) for a given deformation [i.e., a' , b' , c' , or equivalently ω_1 , ω_2 , ω_3 , see Eq. (32)] to solve for the single-particle spectrum ($\tilde{\epsilon}_i$).
4. Evaluate the average, \tilde{E}_{sp} , of the single-particle spectrum according to Eq. (34) and subsequent remarks.
5. Use the results of steps 3 and 4 above to calculate the shell correction $\Delta E_{\text{sh}}^{\text{Str}}$ according to Eq. (14).
6. Finally, calculate the total energy E_{total} as the sum of the liquid-drop contribution (step 2) and the shell correction (step 5), namely $E_{\text{total}} = \tilde{E} + \Delta E_{\text{sh}}^{\text{Str}}$.

The optimal ellipsoidal geometries for a given cluster $M_N^{Z\pm}$, either neutral or charged, are determined by systematically varying the distortion (namely, the parameters a and b) in order to locate the global minimum of the total energy $E_{\text{total}}(N, Z)$ (for the global minima and equilibrium shapes of neutral Na_N clusters according to the ellipsoidal model in the range $3 \leq N \leq 60$, see Fig. 22 of Ref. [40a]).

6. Asymmetric two-center oscillator model for fission

Naturally, the one-center Nilsson oscillator is not the most appropriate empirical potential for describing binary fission, which involves the gradual emergence of two separate fragments. A better choice is the asymmetric two-center oscillator model (ATCOM). According to the ATCOM approach, the single-particle levels, associated with both the initial one-fragment parent and the separated daughters emerging from binary cluster fission, are determined by the following single-particle hamiltonian [69,70],

$$H = T + \frac{1}{2}m_e\omega_{\rho i}^2\rho^2 + \frac{1}{2}m_e\omega_{zi}^2(z - z_i)^2 + V_{\text{neck}}(z) + U(\mathbf{l}_i^2), \quad (36)$$

where $i = 1$ for $z < 0$ (left) and $i = 2$ for $z > 0$ (right).

This hamiltonian is axially symmetric along the z axis. ρ denotes the cylindrical coordinate perpendicular to the symmetry axis [71]. The shapes described by this Hamiltonian are those of two semispheroids (either prolate or oblate) connected by a smooth neck [which is specified by the term $V_{\text{neck}}(z)$]. $z_1 < 0$ and $z_2 > 0$ are the centers of these semispheroids. For the smooth neck, the following 4th-order expression [70] was adopted, namely

$$V_{\text{neck}}(z) = \frac{1}{2}m_e\xi_i\omega_{zi}^2(z - z_i)^4\theta(|z| - |z_i|), \quad (37)$$

where $\theta(x) = 0$ for $x > 0$ and $\theta(x) = 1$ for $x < 0$ and $\xi_i = -1/2z_i^2$.

The frequency $\omega_{\rho i}$ in Eq. (36) must be z -dependent in order to interpolate smoothly between the values $\omega_{\rho i}^\circ$ of the lateral frequencies associated with the left ($i = 1$) and right ($i = 2$) semispheroids, which are not equal in asymmetric cases. The frequencies $\omega_{\rho i}^\circ$ ($i = 1, 2$) characterize the lateral harmonic potentials associated with the two semispheroids outside the neck region. In the implementation of such an interpolation, we follow Ref. [70].

The angular-momentum dependent term $U(\mathbf{l}_i^2)$, where \mathbf{l}_1 and \mathbf{l}_2 are pseudoangular momenta with respect to the left and right centers z_1 and z_2 , is a direct generalization of the corresponding term familiar from the one-center Nilsson potential (e.g., see Ref. [40a]). Its function is to lift the usual harmonic-oscillator degeneracies for different angular momenta, that is, for a spherical shape the $1d - 2s$ degeneracy is properly lifted into a $1d$ shell that is lower than the $2s$ shell (for the parameters entering into this term, which ensure a proper transition from the case of the fissioning cluster to that of the separated two fragments, we have followed Ref. [70]).

The cluster shapes associated with the spatial-coordinate-dependent single-particle potential $V(\rho, z)$ in the hamiltonian (36) (i.e., the second, third, and fourth terms) are determined by the assumption that the cluster surface coincides with an equipotential surface of value V_0 , namely, from the relation $V(\rho, z) = V_0$. Subsequently, one solves for ρ and derives the cluster shape $\rho = \rho(z)$. For the proper value of V_0 , we take the one associated with a spherical shape containing the same number of atoms, N , as the parent cluster, namely, $V_0 = \frac{1}{2}m_e\omega_0^2R^2$, where $\hbar\omega_0 = 49r_s^{-2}N^{-1/3}$ eV, $R = r_sN^{1/3}$, and r_s is the Wigner-Seitz radius in atomic units (monovalent metals have been assumed). Volume conservation is implemented by requiring that the volume enclosed by the fissioning cluster surface (even after separation) remains equal to $4\pi R^3/3$.

The cluster shape in this parametrization is specified by four independent parameters. We take them to be: the separation $d = z_2 - z_1$ of the semispheroids; the asymmetry ratio $q_{as} = \omega_{\rho 2}^\circ/\omega_{\rho 1}^\circ$; and the deformation ratios for the left (1) and right (2) semispheroids $q_i = \omega_{zi}/\omega_{\rho i}^\circ$ ($i = 1, 2$).

The single-particle levels of the hamiltonian in Eq. (36) are obtained by numerical diagonalization in a basis consisting of the eigenstates of the following auxiliary hamiltonian:

$$H_0 = T + \frac{1}{2}m_e\bar{\omega}_\rho^2\rho^2 + \frac{1}{2}m_e\omega_{zi}^2(z - z_i)^2, \quad (38)$$

where $\bar{\omega}_\rho$ is the arithmetic average of $\omega_{\rho 1}^\circ$ and $\omega_{\rho 2}^\circ$. The eigenvalue problem specified by the auxiliary hamiltonian (38) is separable in the cylindrical variables ρ and z . The general solutions in ρ are those of a two-dimensional oscillator, while in z they can be expressed through the parabolic cylinder functions [72]. The matching conditions at $z = 0$ for the left and right domains yield the z -eigenvalues and the associated eigenfunctions [69].

Having obtained the single-particle spectra, the empirical shell correction (in the spirit of Strutinsky's method [38]), $\Delta E_{\text{sh}}^{\text{Str}}$, is determined from Eq. (14).

The single-particle average, $E_{\text{av}}^{\text{Str}}$ [i.e., \tilde{E}_{sp} in Eq. (14)], is calculated [73] through an \hbar expansion of the semiclassical partition function introduced by Wigner and Kirkwood (see references in Ref. [73]). For general-shape potentials, this last method amounts [73] to eliminating the semiclassical Fermi energy $\tilde{\lambda}$ from the set of the following two equations

$$N_e = \frac{1}{3\pi^2} \left(\frac{2m_e}{\hbar^2} \right)^{3/2} \int^{\mathbf{r}_{\tilde{\lambda}}} d\mathbf{r} \left[(\tilde{\lambda} - V)^{3/2} - \frac{1}{16} \frac{\hbar^2}{2m_e} (\tilde{\lambda} - V)^{-1/2} \nabla^2 V \right], \quad (39)$$

and

$$E_{\text{av}}^{\text{Str}} = \frac{1}{3\pi^2} \left(\frac{2m_e}{\hbar^2} \right)^{3/2} \int^{\mathbf{r}_{\tilde{\lambda}}} d\mathbf{r} \left(\left[\frac{3}{5} (\tilde{\lambda} - V)^{5/2} + V (\tilde{\lambda} - V)^{3/2} \right] + \frac{1}{16} \frac{\hbar^2}{2m_e} \left[(\tilde{\lambda} - V)^{1/2} \nabla^2 V - V (\tilde{\lambda} - V)^{-1/2} \nabla^2 V \right] \right), \quad (40)$$

where N_e is the total number of delocalized valence electrons, and $V(\rho, z)$ is the potential in the single-particle hamiltonian of Eq. (36). The domain of integration is demarcated by the classical turning point $\mathbf{r}_{\tilde{\lambda}}$, such that $V(\mathbf{r}_{\tilde{\lambda}}) = \tilde{\lambda}$.

Finally, from the liquid-drop-model contributions, we retain the two most important ones, namely the surface contribution and the Coulomb repulsion. To determine the surface contribution, we calculate numerically the area of the surface of the fissioning cluster shape, $\rho = \rho(z)$, and multiply it by a surface-tension coefficient specified via an ETF-LDA calculation for spherical jellia [25,39] (or even from experimental values). The Coulomb repulsion is calculated numerically using the assumption of a classical conductor, namely the excess 2 units of positive charge are assumed to be distributed over the surface of the fissioning cluster, and in addition each of the fragments carries one unit of charge upon separation (for a more elaborate application of the LDM to triaxially deformed ground states of neutral and charged metal clusters described via a one-center shape parametrization, see our discussion in section II.B.2 in connection with Eqs. (17-26) and Ref. [40]).

As a result, the total energy E_{total} for a specific fission configuration is given by

$$E_{\text{total}} = E_{\text{LDM}} + \Delta E_{\text{sh}}^{\text{Str}} = E_S + E_C + \Delta E_{\text{sh}}^{\text{Str}}, \quad (41)$$

where E_S and E_C are the surface and Coulomb terms, respectively.

III. EXPERIMENTAL TRENDS AND THEORETICAL INTERPRETATION

In the following, we describe applications of the SE-SCM approach to systematic investigations of the effects of shape deformations on the energetics of fragmentation processes of metal clusters [26,40,41], and to studies of deformations and barriers in fission of charged metal clusters [43]. We mention that, in addition, Strutinsky calculations using phenomenological potentials have been reported for the case of neutral sodium clusters assuming axial symmetry in Refs. [46,47,74], and for the case of fission in Refs. [48,49].

A. Electronic shell effects in monomer and dimer separation energies

Monomer and dimer separation energies associated with the unimolecular reactions $K_N^+ \rightarrow K_{N-1}^+ + K$, $K_N^+ \rightarrow K_{N-2}^+ + K_2$, and $\text{Na}_N^+ \rightarrow \text{Na}_{N-1}^+ + \text{Na}$ can be calculated as follows

$$D_{1,N}^+ = E_{\text{total}}(\mathcal{Z} = +1, N - 1) + E_{\text{total}}(\mathcal{Z} = 0, N = 1) - E_{\text{total}}(\mathcal{Z} = +1, N), \quad (42)$$

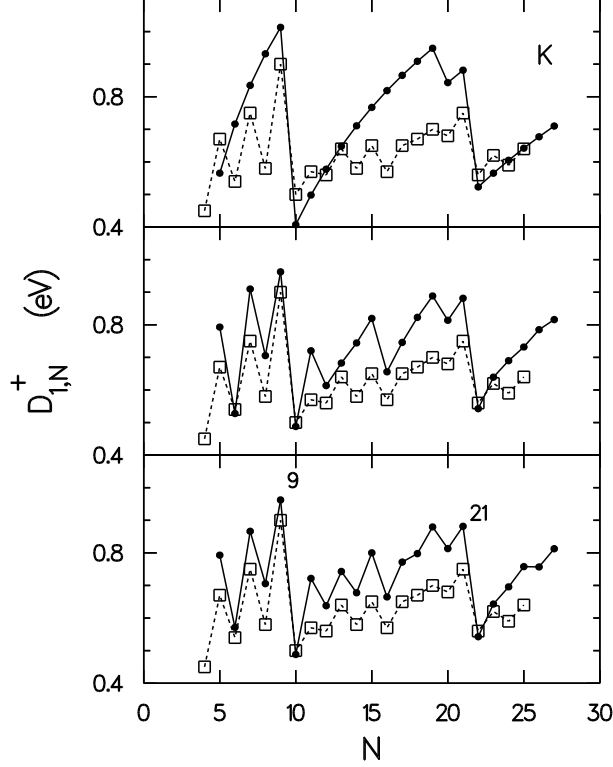


FIG. 2. Monomer separation energies, $D_{1,N}^+$ [see Eq. (42)], from singly cationic K_N^+ clusters in the range $5 \leq N \leq 27$. Solid dots: Theoretical results derived from the SE-SCM method. Open squares: Experimental measurements from Ref. [75]. Top panel: The spherical model compared to experimental data. Middle panel: The spheroidal (axially symmetric) model compared to experimental data. Lower panel: The ellipsoidal (triaxial) model compared to experimental data.

and

$$D_{2,N}^+ = E_{\text{total}}(\mathcal{Z} = +1, N - 2) + E_{\text{total}}(\mathcal{Z} = 0, N = 2) - E_{\text{total}}(\mathcal{Z} = +1, N), \quad (43)$$

where $\mathcal{Z} = \pm Z$ (Z being the excess positive or negative charge in absolute units).

The theoretical results for $D_{1,N}^+$ and $D_{2,N}^+$ for potassium are displayed in Fig. 2 and Fig. 3, respectively, and are compared to the experimental measurements [75]. The theoretical and experimental [76] results for $D_{1,N}^+$ in the case of sodium are displayed in Fig. 4 (bottom panel). An inspection of all three figures leads to the same conclusion as in the case of IPs and electron affinities (see Fig. 1 and Ref. [40a]), i.e., that results obtained via calculations restricted to spherical shapes compare rather poorly with the experiment, that improvement is evident when spheroidal (axially symmetric) deformations are considered, and that the agreement between theory and experiment becomes detailed when triaxiality (i.e., ellipsoidal shapes) is taken into consideration. The feature of the appearance of strong odd-even alternations for $N = 12 - 15$ together with a well-defined quartet in the range $N = 16 - 19$ is present in the experimental monomer separation energies of both potassium and sodium clusters, and theoretically it can be accounted for only after the inclusion of triaxial deformations.

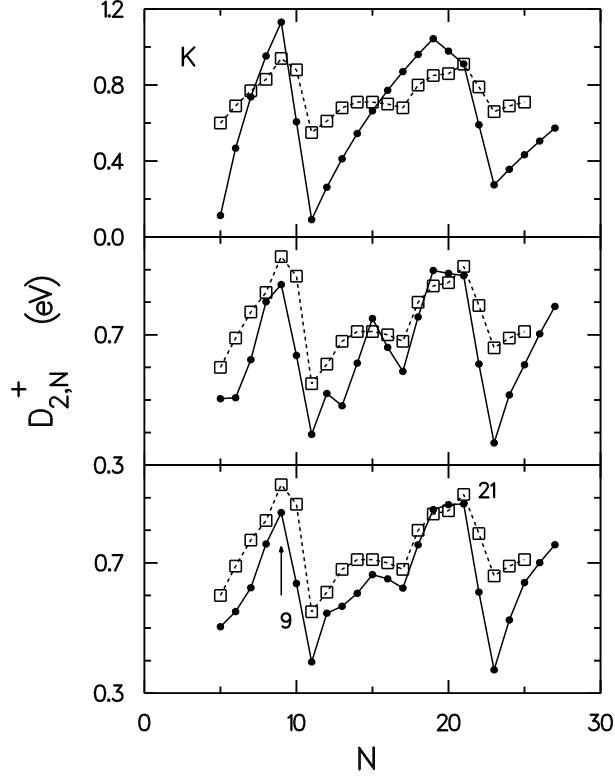


FIG. 3. Dimer separation energies, $D_{2,N}^+$ [see Eq. (43)], from singly cationic K_N^+ clusters in the range $5 \leq N \leq 27$. Solid dots: Theoretical results derived from the SE-SCM method. Open squares: Experimental measurements from Ref. [75]. Top panel: The spherical model compared to experimental data. Middle panel: The spheroidal model compared to experimental data. Lower panel: The ellipsoidal model compared to experimental data.

We note that in the case of dimer separation energies (Fig. 3) the odd-even alternations cancel out. Parents with closed shells or subshells correspond to maxima, while daughters with closed shells or subshells are associated with minima (e.g., the triplets $N = 9 - 11$, or $N = 15 - 17$).

We also include for comparison results obtained by KS-LDA calculations [77] for deformed Na_N clusters restricted to spheroidal (axial) symmetry (Fig. 4, top panel). As expected, except for very small clusters ($N < 9$), these results do not exhibit odd-even oscillations. In addition, significant discrepancies between the calculated and experimental results are evident, particularly pertaining to the amplitude of oscillations at shell and subshell closures.

B. Electronic shell effects in fission energetics

Fission of doubly charged metal clusters, $M_N^{2\pm}$, has attracted considerable attention in the last few years. LDA calculations for fission energetics have usually been restricted to spherical jellia for both parent and daughters, [78,19] with the exception of molecular-dynamical calculations for sodium [10] and potassium [11] clusters with $N \leq 12$. We

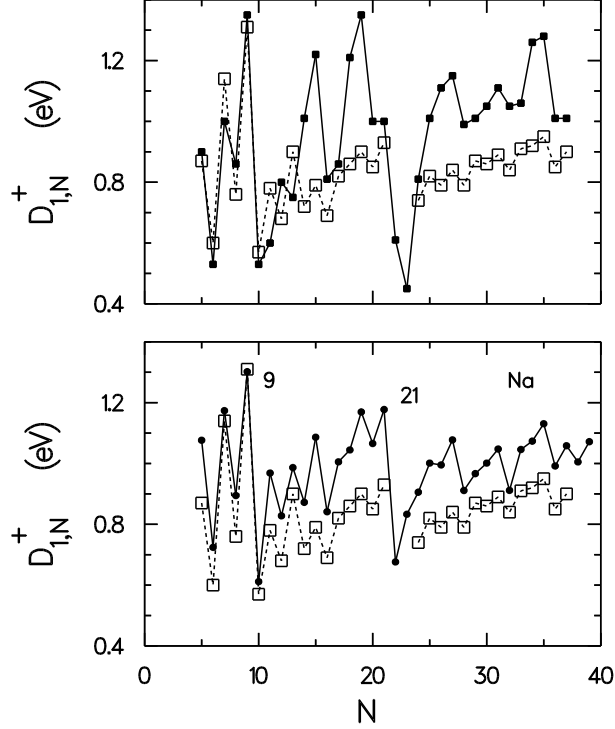


FIG. 4. Monomer separation energies, $D_{1,N}^+$ [see Eq. (42)], from singly cationic Na_N^+ clusters in the range $5 \leq N \leq 39$. Open squares: Experimental measurements from Ref. [76]. Solid dots (Bottom panel): Theoretical results derived from the SE-SCM method in the case of triaxial deformations. Solid squares (Top panel): Theoretical results according to the KS-LDA spheroidal calculations of Ref. [77].

present here systematic calculations for the dissociation energies $\Delta_{N,P}$ of the fission processes $\text{K}_N^{2+} \rightarrow \text{K}_P^+ + \text{K}_{N-P}^+$, as a function of the fission channels P .

We have calculated the dissociation energies

$$\Delta_{N,P} = E_{\text{total}}(\mathcal{Z} = +1, P) + E_{\text{total}}(\mathcal{Z} = +1, N - P) - E_{\text{total}}(\mathcal{Z} = +2, N), \quad (44)$$

for the cases of parent clusters having $N = 26, 23, 18$, and 15 potassium atoms, and compared them with experimental results [79]. The theoretical calculations compared to the experimental results are displayed in Figs. (5 – 8) for $N = 26, 23, 18, 15$, respectively. Again, while consideration of spheroidal shapes improves greatly the agreement between theory and experiment over the spherical model, fully detailed correspondence is achieved only upon allowing for triaxial-shape deformations (notice the improvement in the range $P = 12 - 14$ for $N = 26$, and in the range $P = 10 - 13$ for $N = 23$). In the cases $N = 18$ and $N = 15$ (Fig. 7 and Fig. 8), the biaxial and triaxial results are essentially identical, since no fragment with more than nine electrons is involved. We note that the magic fragments K_3^+ and K_9^+ correspond always to strong minima, and that for $N = 18$ the channel associated with the double magic fragments ($\text{K}_9^+, \text{K}_9^+$) is clearly the favored one over the other magic channel with K_3^+ , in agreement with the experimental analysis.

Finally, we carried out calculations of dissociation energies, Δ_f^{pos} and Δ_f^{neg} , of the most favored fission channels over the whole range up to $N = 100$ atoms for the cases of doubly

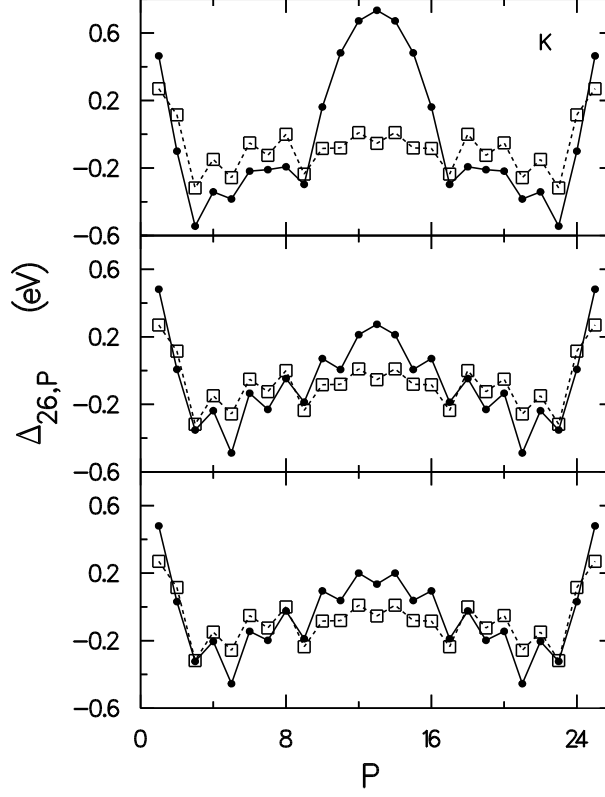


FIG. 5. Fission dissociation energies, $\Delta_{26,P}$ [see Eq. (44)], for the doubly cationic K_{26}^{2+} cluster as a function of the fission channels P . Solid dots: Theoretical results derived from the SE-SCM method. Open squares: Experimental measurements from Ref. [79]. Top panel: The spherical model compared to experimental data. Middle panel: The spheroidal model compared to experimental data. Lower panel: The ellipsoidal model compared to experimental data.

charged cationic and anionic sodium clusters, respectively. The triaxial results compared to the spherical-jellium calculations according to the LDA-SCM method [25] are displayed in Fig. 9 and Fig. 10. In both cases, the main difference from the spherical jellium is a strong suppression of the local minima, indicating that the critical size for exothermic fission is significantly smaller than $N = 100$ (about $N = 30$), as indeed has been observed experimentally for hot cationic alkali-metal clusters [79] (the spherical-jellium results clearly are not compatible with the emergence of such experimental critical sizes in the size range $N \leq 100$).

C. Electronic shell effects in fission barriers and fission dynamics of metal clusters

In this section, we focus our discussion on recent trends in studies of binary fission processes in doubly charged metal clusters.

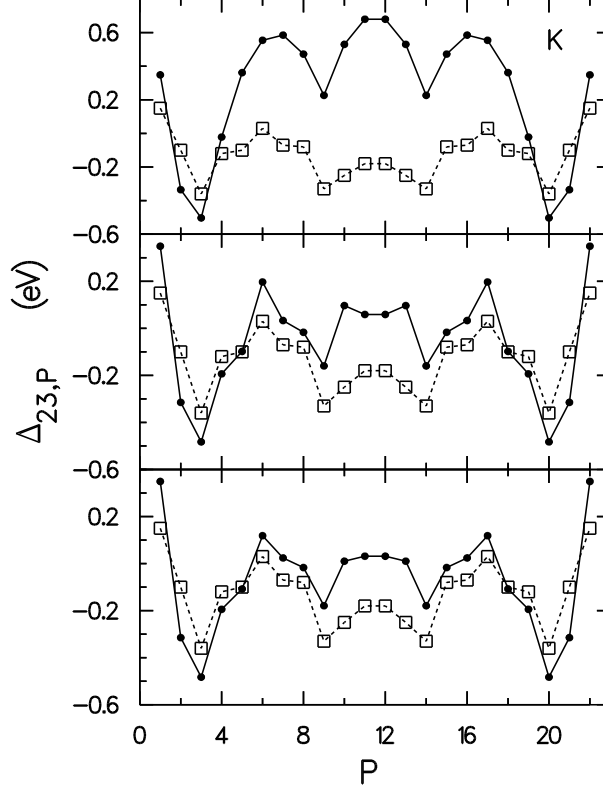


FIG. 6. Fission dissociation energies, $\Delta_{23,P}$ [see Eq. (44)], for the doubly cationic K_{23}^{2+} cluster as a function of the fission channels P . Solid dots: Theoretical results derived from the SE-SCM method. Open squares: Experimental measurements from Ref. [79]. Top panel: The spherical model compared to experimental data. Middle panel: The spheroidal model compared to experimental data. Lower panel: The ellipsoidal model compared to experimental data.

1. Molecular-dynamics studies of fission

Before discussing applications of the SE-SCM (and variants thereof) to the description of cluster fission, we note that for atomic and molecular clusters microscopic descriptions of energetics and dynamics of fission processes, based on modern electronic structure calculations in conjunction with molecular dynamics simulations (where the classical trajectories of the ions, moving on the concurrently calculated Born-Oppenheimer (BO) electronic potential energy surface, are obtained via integration of the Newtonian equations of motion), are possible and have been performed [10,11] using the BO-local-spin-density(-LSD)-functional-MD method [80]. Such calculations, using norm-conserving non-local pseudopotentials and self-consistent solutions of the KS-LSD equations [10,11], applied to small sodium [10] and potassium [11] clusters, revealed several important trends (Figs. 11 – 13): (i) The energetically favorable fission channel for such doubly-charged clusters is the asymmetric one, $M_N^{2+} \rightarrow M_{N-3}^+ + M_3^+$, containing a "magic" daughter M_3^+ ($M = \text{Na}, \text{K}$), i.e., $\Delta_{N,P} = E(M_{N-P}^+) + E(M_P^+) - E(M_N^{2+})$ is smallest for $P = 3$; (ii) Fission of clusters with $N \geq N_b^{2+}$, where $N_b^{2+} = 7$, involves barriers, whose magnitudes reflect the closed-shell stability of the parent cluster (i.e., E_b for $N = 10$ is particularly high), exhibiting a double-

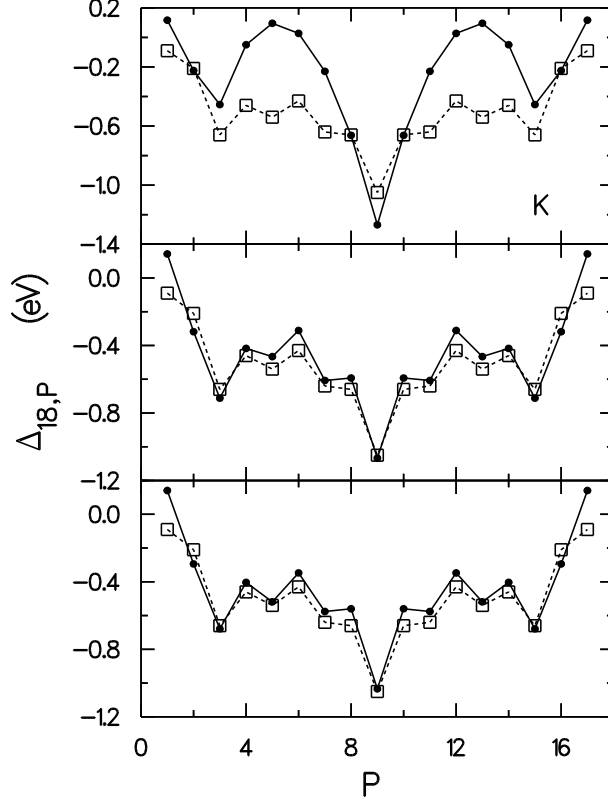


FIG. 7. Fission dissociation energies, $\Delta_{18,P}$ [see Eq. (44)], for the doubly cationic K_{18}^{2+} cluster as a function of the fission channels P . Solid dots: Theoretical results derived from the SE-SCM method. Open squares: Experimental measurements from Ref. [79]. Top panel: The spherical model compared to experimental data. Middle panel: The spheroidal model compared to experimental data. Lower panel: The ellipsoidal model compared to experimental data.

humped barrier shape [see, Figs. 11 and 13(a)]; (iii) The eventual fission products may be distinguishable (i.e., preformed) already at a rather early stage of the fission process (on the top of the exit barrier for Na_{10}^{2+} , see Fig. 12, or prior to the exit barrier for K_{12}^{2+} , see Fig. 13), and the electronic binding between the two fragments is long-range in nature; (iv) The kinetic energy release \mathcal{E}_r in the favorable channel obtained via dynamic simulations was found to be given by $\mathcal{E}_r \approx E_b + |\Delta_{N,3}|$, and the results are in correspondence with experimental measurements [11] for K_N^{2+} ($5 \leq N \leq 12$). Furthermore, in agreement with experimental findings, the emerging fragments are vibrationally excited, with the heating of the internal nuclear degrees of freedom of the fission products in the exit channel originating from dynamical conversion of potential into internal kinetic energy [see, K_{9+}^{int} in Fig. 13(b)].

2. SE-SCM interpretation of fissioning processes

The method we adopt in this section for further studying metal-cluster fission is the SE-SCM described in section II.B.6 (see also Ref. [43]).

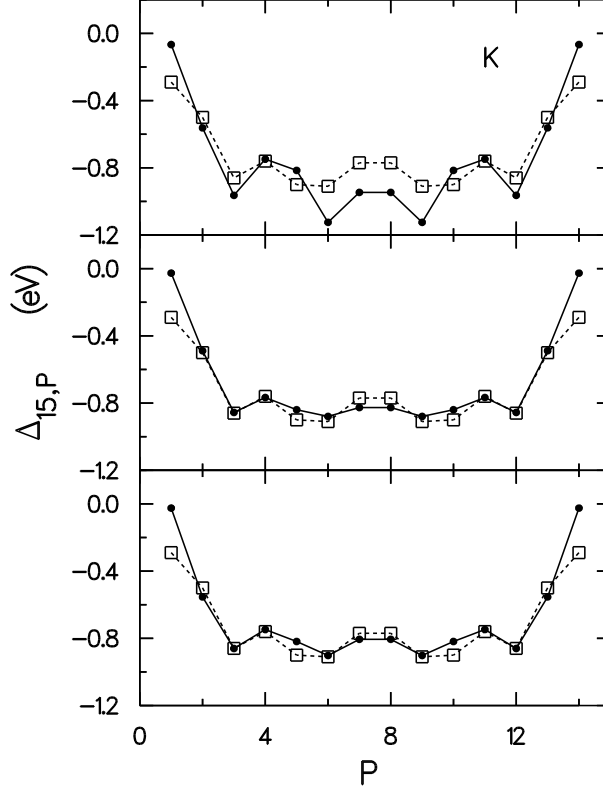


FIG. 8. Fission dissociation energies, $\Delta_{15,P}$ [see Eq. (44)], for the doubly cationic K_{15}^{2+} cluster as a function of the fission channels P . Solid dots: Theoretical results derived from the SE-SCM method. Open squares: Experimental measurements from Ref. [79]. Top panel: The spherical model compared to experimental data. Middle panel: The spheroidal model compared to experimental data. Lower panel: The ellipsoidal model compared to experimental data.

As discussed above (see section II.B), in the SE-SCM method we need to introduce appropriate empirical potentials. As will become apparent from our results, one-center potentials (like the one-center modified, anisotropic harmonic oscillator) are not adequate for describing shell effects in the fission of small metal clusters; rather, a two-center potential is required. Indeed, the empirical potentials should be able to simulate the fragmentation of the initial parent cluster towards a variety of asymptotic daughter-cluster shapes, e.g., two spheres in the case of double magic fragments, a sphere and a spheroid in the case of a single magic fragment, or two spheroids in a more general case. In the case of metal clusters, asymmetric channels are most common, and thus a meaningful and flexible description of the asymmetry is of primary concern. We found [43] that such a required degree of flexibility can be provided via the shape parametrization of the asymmetric two-center-oscillator shell model (ATCOSM) introduced earlier in nuclear fission [69] (see section II.B.6).

In addition to the present shape parametrization [43], other two-center shape parametrizations [mainly in connection with KS-LDA jellium calculations] have been used [81–83] in studies of metal cluster fission. They can be grouped into two categories, namely, the two-intersected-spheres jellium [81,84], and the variable-necking-in parametrizations [82,83]. In the latter group, Ref. [82] accounts for various necking-in situations by using

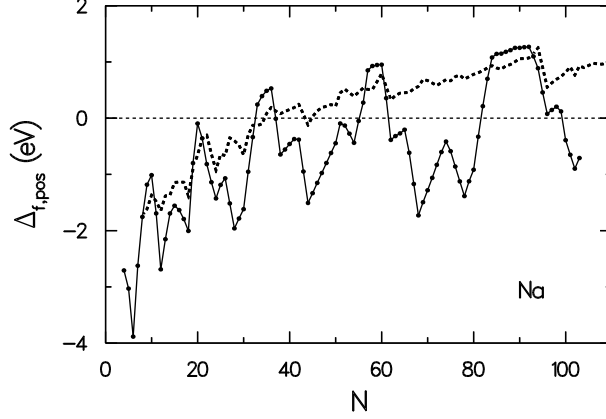


FIG. 9. Solid dots: LDA-SCM results for the dissociation energies Δ_f^{pos} for the most favorable fission channel for doubly charged cationic parents Na_N^{2+} when the spherical jellium is used. The influence of triaxial deformation effects (calculated with the SE-SCM approach) is shown by the thick dashed line.

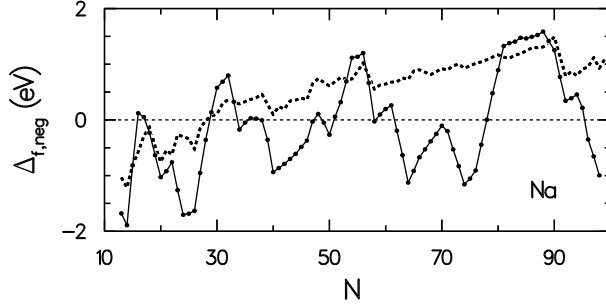


FIG. 10. Solid dots: LDA-SCM results for the dissociation energies Δ_f^{neg} for the most favorable fission channel for doubly charged anionic parents Na_N^{2-} when the spherical jellium is used. The influence of triaxial deformation effects (calculated with the SE-SCM approach) is shown by the thick dashed line.

the "funny-hills" parametrization [85], while Ref. [83] describes the necking-in by connecting two spheres smoothly through a quadratic surface. The limitation of these other parametrizations is that they are not flexible enough to account for the majority of the effects generated by the shell structure of the parent and daughters, which in general do not have spherical, but deformed (independently from each other), shapes. An example is offered by the case of the parent Na_{18}^{2+} , which has a metastable oblate ground state, and thus cannot be described by any one of the above parametrizations. We wish to emphasize again that one of the conclusions of the present work is that the shell structures of the (independently deformed) parent and daughters are the dominant factors specifying the fission barriers, and thus parametrizations [81–83] with restricted final fragment (or parent) shapes are deficient in accounting for some of the most important features governing metal-cluster fission.

As a demonstration of our method, we present results for two different parents, namely Na_{10}^{2+} and Na_{18}^{2+} .

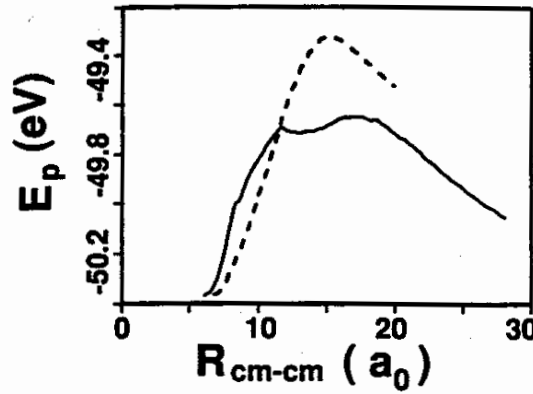


FIG. 11. Molecular dynamics results for the potential energy vs distance (in atomic units) between the centers of mass for the fragmentation of Na_{10}^{2+} into Na_7^+ and Na_3^+ (solid) and Na_9^+ and Na^+ (dashed), obtained via constrained minimization of the LSD ground-state energy of the system [10].

Fig. 14 presents results for the channel $\text{Na}_{10}^{2+} \rightarrow \text{Na}_7^+ + \text{Na}_3^+$ for three different cases, namely, when the larger fragment Na_7^+ is oblate (left column), spherical (middle column), and prolate (right column). From our one-center analysis, we find as expected that Na_7^+ (with six electrons) has an oblate global minimum and a higher in energy prolate local minimum. In the two-center analysis, we have calculated the fission pathways so that the emerging fragments correspond to possible deformed one-center minima. It is apparent that the most favored channel (i.e., having the lowest barrier, see the solid line in the bottom panels) will yield an oblate Na_7^+ (left column in Fig. 14), in agreement with the expectations from the one-center energetics analysis.

The middle panels exhibit the decomposition of the total barrier into the three components of surface, Coulomb, and shell-correction terms [see Eq. (41)], which are denoted by an upper dashed curve, a lower dashed curve, and a solid line, respectively. The total LDM contribution (surface plus Coulomb) is also exhibited at the bottom panels (dashed lines).

It can be seen that the LDM barrier is either absent or very small, and that the total barrier is due almost exclusively to electronic shell effects. The total barrier has a double-humped structure, with the outer hump corresponding to the LDM saddle point, which also happens to be the scission point (indicated by an empty vertical arrow). The inner hump coincides with the peak of the shell-effect term, and is associated with the rearrangement of single-particle levels from the initial spherical parent to a molecular configuration resembling a Na_7^+ attached to a Na_3^+ . Such molecular configurations (discovered earlier in first-principles MD simulations [10,11] of fission of charged metal clusters, as well as in studies of fusion of neutral clusters [86]) are a natural precursor towards full fragment separation and complete fission, and naturally they give rise to the notion of preformation of the emerging fragments [10,11].

Fig. 15(a) displays the ATCOSM results for the symmetric channel $\text{Na}_{18}^{2+} \rightarrow 2\text{Na}_9^+$, when, for illustrative purposes, the parent is assumed to be spherical at $d = 0$ (this channel is

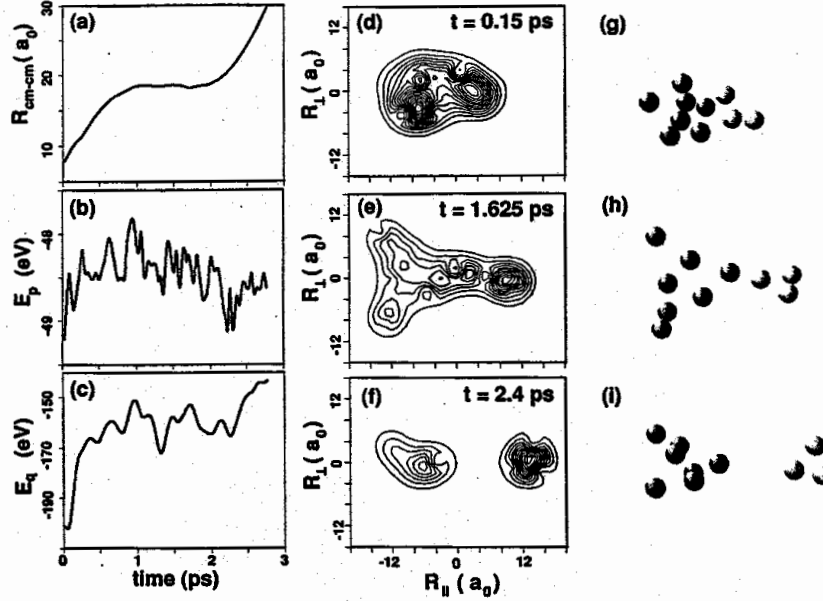


FIG. 12. Fragmentation dynamics of Na_{10}^{2+} from first-principles Born-Oppenheimer Local-spin-density functional Molecular-dynamics simulations [10]. (a)-(c) Center-of-mass distance between the eventual fission products ($R_{\text{c.m.-c.m.}}$), total potential energy (E_p), and the electronic contribution E_q to E_p , vs time. (d)-(f) Contours of the total electronic charge distribution at selected times calculated in the plane containing the two centers of mass. The R_{\parallel} axis is parallel to $\mathbf{R}_{\text{c.m.-c.m.}}$. (g)-(i) Cluster configurations for the times given in (d)-(f). Dark and light balls represent ions in the large and small fragments, respectively. Energy, distance, and time in units of eV, bohr (a_0), and ps, respectively.

favorable compared to that of the trimer [43], both from energetics and barrier considerations; for small clusters, this is the only case where a channel other than that of the trimer is the most favored one). The top panel of Fig. 15(a) describes the evolution of the single-particle spectra. The spherical ordering $1s$, $1p$, $1d$, $2s$, etc., for the parent at $d = 0$ is clearly discernible. With increasing separation distance, the levels exhibit several crossings, and, after the scission point, they naturally regroup to a new ordering associated with the spherical Na_9^+ products (at the end of the fission process, the levels are doubly degenerate compared to the initial configuration, since there are two Na_9^+ fragments). It is seen that the ATCOSM leads to an oscillator energy (i.e., the gap between two populated major shells exhibited at the right end of the figure) of 1.47 eV for each Na_9^+ fragment in agreement with the value expected from the one-center model [the $1s$ state of Na_9^+ lies at 2.21 eV; in the case of the initial spherical Na_{18}^{2+} ($d = 0$), the oscillator energy corresponding to the

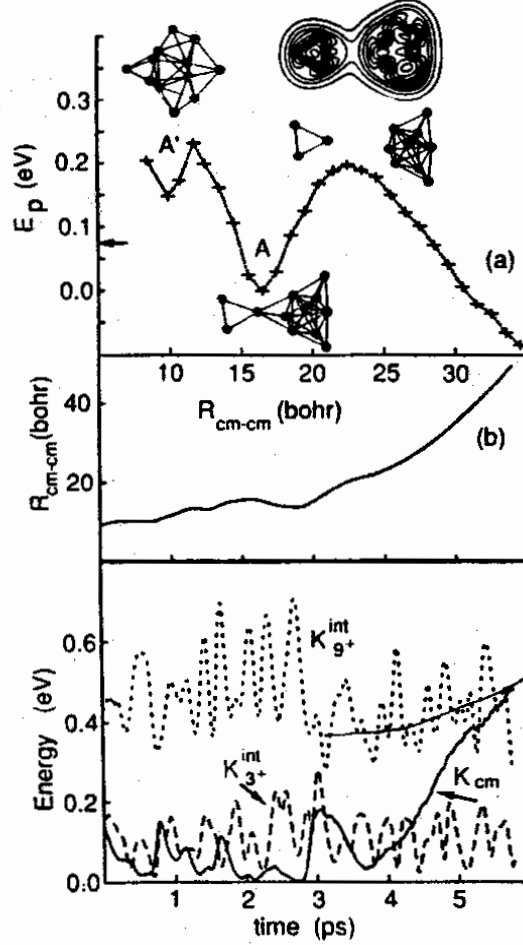


FIG. 13. (a) Potential energy of K_{12}^{2+} fissioning in the favorable channel ($K_3^+ + K_9^+$) versus the inter-fragment distance R_{cm-cm} , obtained via constrained minimization. The origin of the E_p scale is set at the optimal pre-barrier configuration (A). For large R_{cm-cm} , $E_p = -0.9$ eV, i.e., Δ_3 . Included also are cluster configurations of K_{12}^{2+} corresponding to: a compact isomer (A') (the energy of the optimal compact isomer found is denoted by an arrow); the optimal bound configuration (A); the structure on top of the exit-channel barrier for which contours of the total electronic charge density, ρ , are shown [11].

(b) Time evolution of R_{cm-cm} , the internal vibrational kinetic energies of the fragments (K_{3+}^{int} and K_{9+}^{int}) and the sum of the fragments translational kinetic energies (K_{cm}) obtained via a BO-LSD-MD simulation starting from ionization ($t = 0$) of a K_{12}^+ cluster at 500 K. A line is drawn in K_{9+}^{int} (for $t \geq 3$ ps) to guide the eye, illustrating heating of the internal vibrational degrees of freedom of the departing fragment.

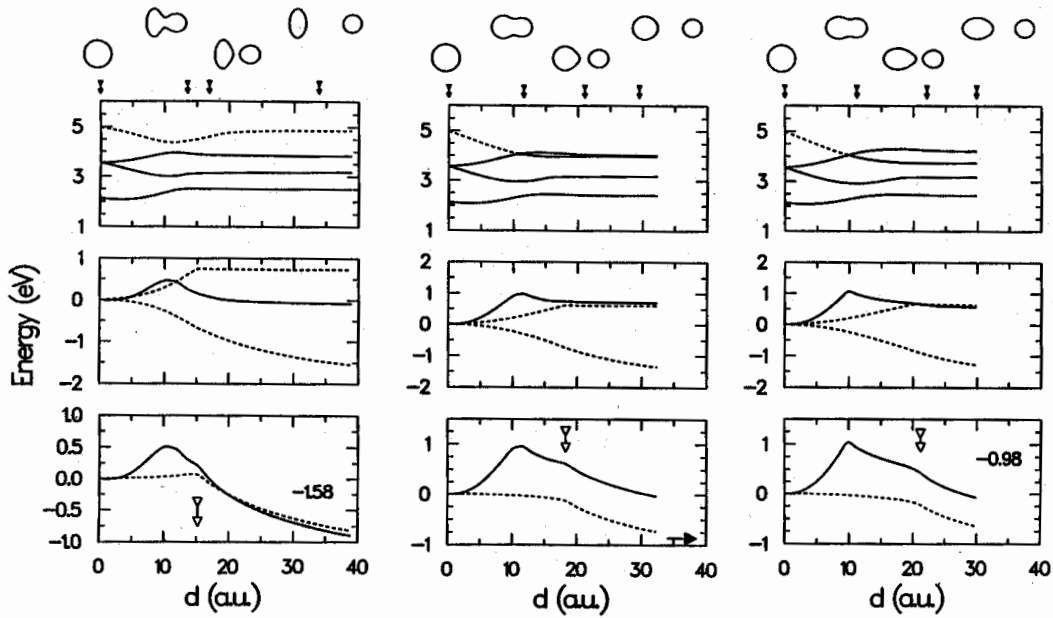


FIG. 14. ATCOSM results for the asymmetric channel $\text{Na}_{10}^{2+} \rightarrow \text{Na}_7^+ + \text{Na}_3^+$. The final configuration of Na_3^+ is spherical. For the heavier fragment Na_7^+ , we present results associated with three different final shape configurations, namely, oblate [(o,s); left], spherical [(s,s); middle], and prolate [(p,s); right]. The ratio of shorter over longer axis is 0.555 for the oblate case and 0.75 for the prolate case.

Bottom panel: LDM energy (surface plus Coulomb, dashed curve) and total potential energy (LDM plus shell corrections, solid curve) as a function of fragment separation d . The empty vertical arrow marks the scission point. The zero of energy is taken at $d = 0$. A number (-1.58 eV or -0.98 eV), or a horizontal solid arrow, denotes the corresponding dissociation energy.

Middle panel: Shell-correction contribution (solid curve), surface contribution (upper dashed curve), and Coulomb contribution (lower dashed curve) to the total energy, as a function of fragment separation d .

Top panel: Single-particle spectra as a function of fragment separation d . The occupied (fully or partially) levels are denoted with solid lines. The unoccupied levels are denoted with dashed lines. On top of the figure, four snapshots of the evolving cluster shapes are displayed. The solid vertical arrows mark the corresponding fragment separations. Observe that the doorway molecular configurations correspond to the second snapshot from the left. Notice the change in energy scale for the middle and bottom panels, as one passes from (o,s) to (s,s) and (p,s) final configurations.

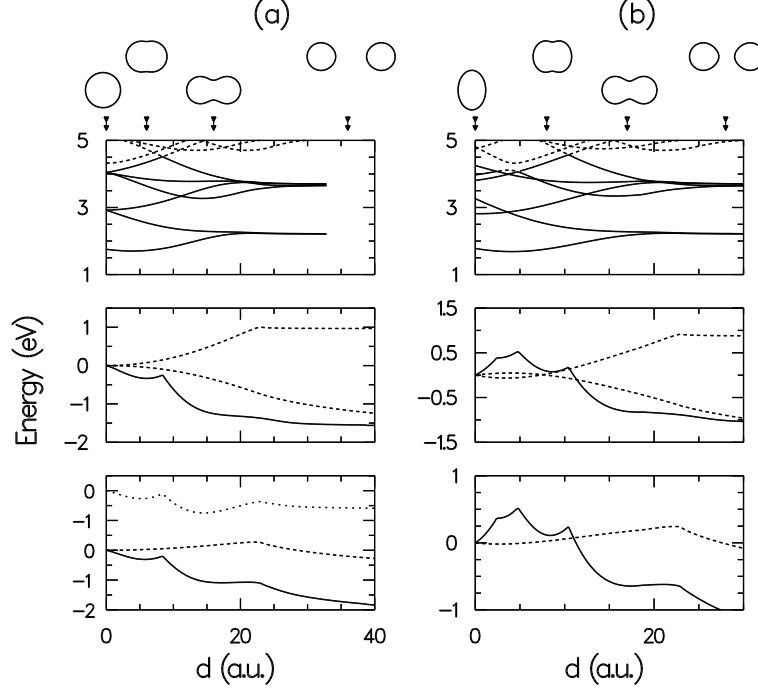


FIG. 15. ATCOSM results for the symmetric channel $\text{Na}_{18}^{2+} \rightarrow 2\text{Na}_9^+$, when the initial parent shape is assumed (a) spherical, and (b) oblate (with a shorter over longer axis ratio equal to 0.699). Panel distribution and other notations and conventions are the same as in Fig. 14. The top dotted line in the bottom panel of (a) represents the total energy without the Coulomb contribution. Observe that the doorway molecular configurations correspond to the third snapshot from the left. Notice that the zero of all energies is taken at $d = 0$.

gap between major shells is 1.17 eV, and the corresponding $1s$ state lies at 1.75 eV].

From the middle panel of Fig. 15(a), we observe that the shell-correction (solid line) contributes a net gain in energy of about 1.6 eV upon dissociation into two Na_9^+ fragments. This gain is larger than the increase in energy (i.e., positive energy change) due to the surface term, which saturates at a value of about 1 eV after the scission point at $d \approx 23$ a.u. The total energy is displayed in the bottom panel of Fig. 15(a) (solid line) along with the LDM barrier (dashed line). Even though distorted (when compared to the cases of Fig. 14), the total barrier still exhibits a two-peak structure, the inner peak arising from the hump in the shell correction, and the outer peak arising from the point of saturation of the surface term (this last point coincides again with the scission point, as well as with the saddle of the LDM barrier). An inner local minimum is located at $d \approx 8$ a.u., and corresponds to a compact prolate shape of the parent [see second drawing from the left at the top of Fig. 15(a)], while a second deeper minimum appears at $d \approx 18$ a.u., corresponding to a superdeformed shape of a molecular configuration of two Na_9^+ clusters tied up together [preformation of fragments, see third drawing from the left at the top of Fig. 15(a)]. The inner barrier separating the compact prolate configuration from the superdeformed molecular configuration arises from the rearrangement of the single-particle levels during the transition from the initially assumed spherical Na_{18}^{2+} configuration to that of the supermolecule $\text{Na}_9^+ + \text{Na}_9^+$. We note that the barrier separating the molecular configuration from complete fission is very weak

being less than 0.1 eV.

The top dotted line at the bottom panel displays the total energy in the case when the Coulomb contribution is neglected. This curve mimics the total energy for the fusion of two neutral Na_8 clusters, namely the total energy for the reaction $2\text{Na}_8 \rightarrow \text{Na}_{16}$. Overall, we find good agreement with a KS-LDA calculation for this fusion process (see Fig. 1 of Ref. [86]). We further note that the superdeformed minimum for the neutral Na_{16} cluster is deeper than that in the case of the doubly charged Na_{18}^{2+} cluster. Naturally, this is due to the absence of the Coulomb term.

The natural way for producing experimentally the metastable Na_{18}^{2+} cluster is by ionization of the stable singly-charged Na_{18}^+ cluster. Since this latter cluster contains seventeen electrons and has a deformed oblate ground state [40a], it is not likely that the initial configuration of Na_{18}^{2+} will be spherical or prolate as was assumed for illustration purposes in Fig. 15(a). Most likely, the initial configuration for Na_{18}^{2+} will be that of the oblate Na_{18}^+ . To study the effect that such an oblate initial configuration has on the fission barrier, we display in Fig. 15(b) ATCOSM results for the pathway for the symmetric fission channel, starting from an oblate shape of Na_{18}^{2+} , proceeding to a compact prolate shape, and then to full separation between the fragments via a superdeformed molecular configuration. We observe that additional potential humps (in the range $2 \text{ a.u.} \leq d \leq 6 \text{ a.u.}$), associated with the shape transition from the oblate to the compact prolate shape, do develop. Concerning the total energies, the additional innermost humps result in the emergence of a significant fission barrier of about 0.52 eV for the favored symmetric channel [see $d \approx 5 \text{ a.u.}$ in Fig. 15(b)].

From the above analysis, we conclude that considerations of the energy pathways leading from the parent to preformation configurations (i.e., the inner-barrier hump, or humps) together with the subsequent separation processes are most important for proper elucidation of the mechanisms of metal-cluster fission processes. This corroborates earlier results obtained via first-principles MD simulations [10,11] pertaining to the energetics and dynamical evolution of fission processes, and emphasizes that focusing exclusively [81,83] on the separation process between the preformed state and the ultimate fission products provides a rather incomplete description of fission phenomena in metal clusters. It is anticipated that, with the use of emerging fast spectroscopies [87], experimental probing of the detailed dynamics of such fission processes could be achieved.

IV. INFLUENCE OF ELECTRONIC ENTROPY ON SHELL EFFECTS

In the previous sections, we showed that consideration of triaxial (ellipsoidal) shapes in the framework of the SCM leads to overall substantial systematic improvement in the agreement between theory and experimental observations pertaining to the major and the fine structure of the size-evolutionary patterns associated with the energetics of fragmentation processes (monomer/dimer dissociation energies and fission energetics) and ionization.

The theoretical methods and discussion of deformation effects in the previous sections were restricted to zero temperature. However, the experiments are necessarily made with clusters at finite temperatures, a fact that strongly motivates the development of finite-temperature theoretical approaches.

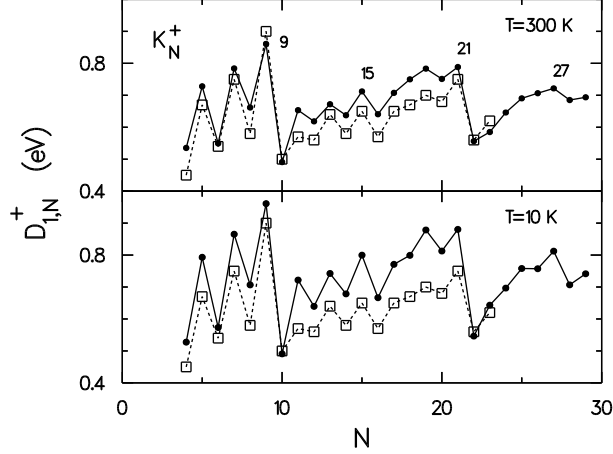


FIG. 16. Monomer separation energies of K_N^+ clusters at two temperatures, $T = 10$ K, and 300 K. Solid dots: Theoretical FT-SE-SCM results. Open squares: experimental measurements [75]. To facilitate comparison, the SE-SCM results at the higher temperature have been shifted by 0.07 eV, so that the theoretical curves at both temperatures refer to the same point at $N = 10$.

Due to the difficulty of the subject, to date only a few finite-temperature theoretical studies of metal clusters have been performed. In this section, we discuss briefly some of the conclusions of a recent SCM study [41] regarding the importance of thermal effects. The theoretical details pertaining to this finite-temperature (FT) –SE–SCM will not be elaborated here, but they can be found in the aforementioned reference.

The main conclusion of Ref. [41] was that, in conjunction with deformation effects, electronic-entropy effects in the size-evolutionary patterns of relatively small (as small as 20 atoms) simple-metal clusters become prominent already at moderate temperatures. At smaller sizes, electronic-entropy effects are less prominent, but they can still be discernible. As an example, we present in Fig. 16 the monomer separation energies of K_N^+ clusters for two temperatures ($T = 10$ K and $T = 300$ K), along with the available experimental measurements [75] (open squares) in the size range $N = 4 - 23$. First notice that the $T = 10$ K results are practically indistinguishable from the $T = 0$ K results presented in Fig. 2. Compared to the $T = 10$ K results, the theoretical results at $T = 300$ K are in better agreement with the experimental ones due to an attenuation of the amplitude of the alternations (e.g., notice the favorable reduction in the size of the drops at $N = 9, 15$, and 21). This amplitude attenuation, however, is moderate, and it is remarkable that the $T = 300$ K SCM results in this size range preserve in detail the same relative pattern as the $T = 0$ K ones (in particular, the well-defined odd-even oscillations in the range $N = 4 - 15$ and the ascending quartet at $N = 16 - 19$ followed by a dip at $N = 20$).

As a further example, the theoretical IPs of K_N clusters in the size range $3 \leq N \leq 102$ for three temperatures, $T = 10$ K, 300 K, and 500 K, are displayed in Fig. 17, and are compared with the experimental measurements [36] (open squares; the experimental uncertainties are 0.06 eV for $N \leq 30$ and 0.03 eV for $N > 30$). As was the case with our earlier $T = 0$ K results [40], the $T = 10$ K theoretical results exhibit the following two characteristics: (i) Above $N = 21$, a pronounced fine structure between major-shell closures which is not present in the experimental measurements; (ii) Steps at the major-shell closures which are

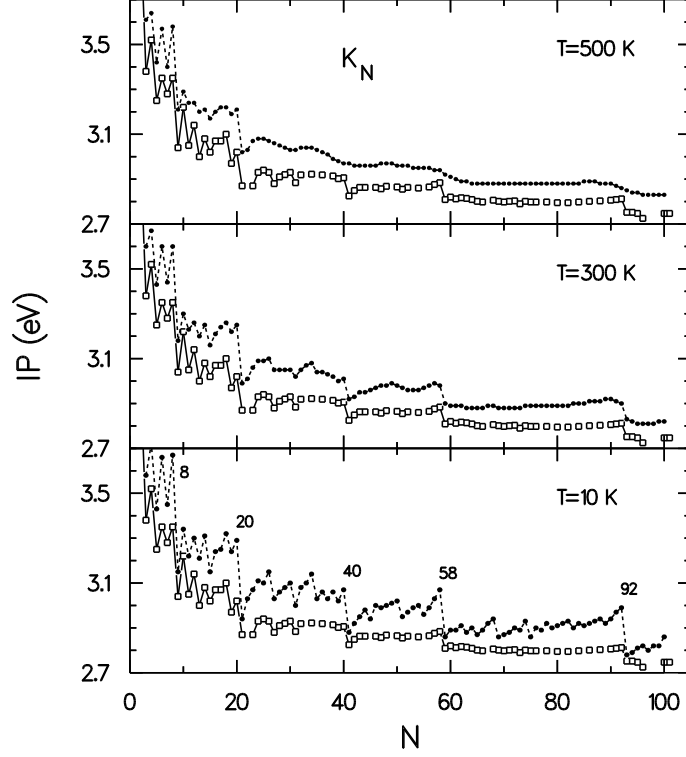


FIG. 17. IPs of K_N clusters at three temperatures, $T = 10$ K, 300 K, and 500 K. Solid dots: Theoretical FT-SE-SCM results. Open squares: experimental measurements [36].

much larger than the experimental ones, i.e., three-to-five times for $N = 40, 58$, and 92 , and two-to-three times for $N = 8$ and 20 [this needs to be contrasted to the experimental IPs for cold Na_N clusters, which are in overall good agreement with our $T = 0$ K SE-SCM results regarding both characteristics (see Fig. 1)].

The agreement between theory and experiment is significantly improved at $T = 300$ K. Indeed, in comparison with the lower-temperature calculations, the $T = 300$ K results exhibit the following remarkable changes: (i) Above $N = 21$, the previously sharp fine-structure features are smeared out, and as a result, the theoretical curve follows closely the mild modulations of the experimental profile. In the size range $N = 21 - 34$, three rounded, hump-like formations (ending to the right at the subshell closures at $N = 26, 30$, and 34) survive in very good agreement with the experiment (the sizes of the drops at $N = 26, 30$ and 34 are comparable to the experimental ones [88]); (ii) The sizes of the IP drops at $N = 20, 40, 58$, and 92 are reduced drastically and are now comparable to the experimental ones. In the size range $N \leq 20$, the modifications are not as dramatic. Indeed, one can clearly see that the pattern of odd-even alternations remains well defined, but with a moderate attenuation in amplitude, again in excellent agreement with the experimental observation.

For $T = 500$ K, the smearing out of the shell structure associated with the calculated results progresses even further, obliterating the agreement between theory and experiment. Specifically, the steps at the subshell closures at $N = 26$ and 30 , as well as at the major-shell closures at $N = 40, 58$, and 92 are rounded and smeared out over several clusters (an

analogous behavior has been observed in the logarithmic abundance spectra of hot, singly cationic, copper, silver, and gold clusters [89]). At the same time, however, the odd-even alternation remains well defined for $N \leq 8$. We further notice that, while some residue of fine structure survives in the range $N = 9 - 15$, the odd-even alternations there are essentially absent (certain experimental measurements [90] of the IPs of hot Na_N clusters appear to conform to this trend).

The influence of the electronic entropy on the height of fission barriers has not been studied as yet, but it will undoubtedly be the subject of future research in metal-cluster physics. In any case, based on the results of this section, it is natural to conjecture that electronic-entropy effects will tend to quench the barrier heights, especially in the case of larger multiply charged clusters.

V. SUMMARY

In this chapter, we have elucidated certain issues pertaining to evaporation and fission processes of metallic clusters, focusing on electronic shell effects and their importance in determining the energetics, structure, pathways, and dynamical mechanisms of dissociation and fragmentation in these systems, and have outlined and demonstrated various theoretical approaches currently used in investigations of cluster fragmentation phenomena, ranging from microscopic first-principles electronic structure calculations coupled with molecular dynamics simulations to adaptation of more phenomenological in nature models originated in studies of atomic nuclei. In this respect, a recurrent theme in this exposition has been the crucial importance of deformation and electronic-entropy (temperature) effects, as well as their treatment with the help of shell correction methods.

By drawing analogies, as well as differences, between certain aspects of nuclear fission and nuclear radioactivity phenomena and atomic (metallic) cluster fission processes, we have attempted to provide a unifying conceptual framework for discussion of the physical principles underlying modes of cluster fission (i.e., importance of deformations, shell effects originating from fragments and parent, asymmetric and symmetric fission, single and double-humped barriers, fissioning cluster shapes, and dynamical aspects, such as the time-scale of fission processes, kinetic energy release, and dynamical energy redistribution among the fission products).

We conclude by commenting on some experimental and theoretical issues in cluster fission which remain as future challenges (limiting ourselves to metallic clusters). These include: fission dynamics of multiply charged large metal clusters [6,23,24]; systematic investigations of temperature effects on modes of cluster fission, and ternary, and higher multi-fragmentation processes; time-resolved spectroscopy of fission processes and of fission isomers; spin effects in fission; tunneling processes and corresponding life-times in sub-barrier fission modes of clusters of light elements, e.g., lithium; and fission processes of non-simple metal clusters.

This research was supported by a grant from the U.S. Department of Energy (Grant No.

FG05-86ER45234). Calculations were performed on CRAY computers at the Supercomputer Center at Livermore, California, and the Georgia Institute of Technology Center for Computational Materials Science.

REFERENCES

- [1] Å. Bohr and B. R. Mottelson, *Nuclear Structure*, Vol. II (Benjamin, Reading, MA, 1975).
- [2] M. A. Preston and R. K. Bhaduri, *Structure of the Nucleus* (Addison-Wesley, London, 1975).
- [3] W. Frost, *Theory of unimolecular reactions*, (Academic, New York, 1973).
- [4] C. Bréchnignac, Ph. Cahuzac, F. Carlier, M. De Frutos, J. Leygnier, J. Ph. Roux, and A. Sarfati, *Comments At. Mol. Phys.* **31**, 361 (1995), and references therein.
- [5] W. A. Saunders, *Phys. Rev. A* **46**, 7028 (1992).
- [6] T. P. Martin, U. Näher, H. Göhlich, and T. Lange, *Chem. Phys. Lett.* **196**, 113 (1992); U. Näher, H. Göhlich, T. Lange, and T. P. Martin, *Phys. Rev. Lett.* **68**, 3416 (1992).
- [7] The usage of the term fragmentation here should not be confused with the 'fragmentation of the oscillator strength' (also referred to as Landau damping or Landau fragmentation), which is a phenomenon associated with the profile of the photoabsorption cross section of metal clusters, and it may lead to the broadening of the photoabsorption profiles and/or to the appearance of a multipeak profile. It was first described using the matrix-RPA/LDA version of linear response for the case of neutral Na_{20} in C. Yannouleas, R. A. Broglia, M. Brack, and P.-F. Bortignon, *Phys. Rev. Lett.* **63**, 255 (1989). For other metal-cluster species and sizes, see also C. Yannouleas and R. A. Broglia, *Europhys. Lett.* **15**, 843 (1991); C. Yannouleas and R. A. Broglia, *Phys. Rev. A* **44**, 5793 (1991); C. Yannouleas, *Chem. Phys. Lett.* **193**, 587 (1992); C. Yannouleas, P. Jena, and S. N. Khanna, *Phys. Rev. B* **46**, 9751 (1992); C. Yannouleas, E. Vigezzi, and R. A. Broglia, *Phys. Rev. B* **47**, 9849 (1993); C. Yannouleas, F. Catara, and N. Van Giai, *Phys. Rev. B* **51**, 4569 (1995); C. Yannouleas, *Phys. Rev. B* **58**, 6748 (1998).
- [8] For monovalent elements (Na, K, Cu, etc.), N is also equal to the number N_e of delocalized valence electrons.
- [9] (a) C. Bréchnignac, Ph. Cahuzac, F. Carlier, and M. de Frutos, *Phys. Rev. Lett.* **64**, 2893 (1990); (b) C. Bréchnignac, Ph. Cahuzac, F. Carlier, and M. de Frutos, *Phys. Rev. B* **49**, 2825 (1994).
- [10] R. N. Barnett, U. Landman, and G. Rajagopal, *Phys. Rev. Lett.* **67**, 3058 (1991).
- [11] C. Bréchnignac, Ph. Cahuzac, F. Carlier, M. de Frutos, R. N. Barnett, and U. Landman, *Phys. Rev. Lett.* **72**, 1636 (1994).
- [12] N. Bohr and J. A. Wheeler, *Phys. Rev.* **56**, 426 (1939).
- [13] J. R. Nix and W. J. Swiatecki, *Nucl. Phys.* **71**, 1 (1965).
- [14] G. Gamow, *Z. Phys.* **51**, 204 (1928).
- [15] E. U. Condon and R. W. Gurney, *Nature* **122**, 439 (1928).
- [16] A. Sandulescu, D. N. Poenaru, and W. Greiner, *Sov. J. Part. Nucl.* **11**, 528 (1980).
- [17] P. B. Price, *Ann. Rev. Nucl. Part. Sci.* **39**, 19 (1989).
- [18] For a theoretical review, see W. Greiner, M. Ivascu, D. N. Poenaru, and A. Sandulescu, *Cluster radioactivities*, in *Treatise on Heavy-Ion Science*, edited by D.A. Bromley (Plenum, New York, 1989), Vol. 8, p. 641.
- [19] J. M. López, J. A. Alonso, F. Garcias, and M. Barranco, *Ann. Physik (Leipzig)* **1**, 270 (1992).

- [20] S. G. Nilsson, C.-F. Tsang, A. Sobiczewski, Z. Szymanski, S. Wycech, C. Gustafson, I.-L. Lamm, P. Moller, and B. Nilsson, Nucl. Phys. **A131**, 1 (1969).
- [21] W. D. Myers and W. J. Swiatecki, Nucl. Phys. **81**, 1 (1966).
- [22] T. D. Märk and O. Echt, in *Clusters of Atoms and Molecules II*, edited by H. Haberland (Springer-Verlag, Berlin, 1994), ch. 2.6; O. Echt and T. D. Märk, *ibid.* ch. 2.7.
- [23] C. Bréchignac, Ph. Cahuzac, F. Carlier, M. de Frutos, N. Kebaili, J. Leygnier, A. Sarfati, and V. M. Akulin, in *Large Clusters of Atoms and Molecules*, edited by T. P. Martin (Kluwer, Dordrecht, 1996), p. 315.
- [24] U. Näher, S. Frank, N. Malinowski, U. Zimmermann, T. P. Martin, Z. Phys. D **31**, 191 (1994).
- [25] C. Yannouleas and U. Landman, Phys. Rev. B **48**, 8376 (1993); Chem. Phys. Lett. **210**, 437 (1993).
- [26] C. Yannouleas and U. Landman, in *Large Clusters of Atoms and Molecules*, edited by T. P. Martin (Kluwer, Dordrecht, 1996), p. 131.
- [27] M. K. Scheller, R. N. Compton, and L. S. Cederbaum, Science **270**, 1160 (1995).
- [28] C. Yannouleas and U. Landman, Chem. Phys. Lett. **217**, 175 (1994).
- [29] P. Scheier, B. Dunser, R. Worgotter, D. Muigg, S. Matt, O. Echt, M. Foltin, and T. D. Märk, Phys. Rev. Lett. **77**, 2654 (1996).
- [30] D. Scharf, J. Jortner, and U. Landman, J. Chem. Phys. **88**, 4273 (1988).
- [31] D. H. E. Gross, M. E. Madjet, and O. Schapiro, Z. Phys. D **39**, 75 (1997).
- [32] R. N. Barnett and U. Landman, J. Phys. Chem. **99**, 17305 (1995).
- [33] W. Ekardt, Phys. Rev. B **29**, 1558 (1984); Phys. Rev. B **31**, 6360 (1985).
- [34] D. E. Beck, Solid State Commun. **49**, 381 (1984).
- [35] K. L. Clemenger, Phys. Rev. B **32**, 1359 (1985); Ph. D. Dissertation, University of California, Berkeley, 1985.
- [36] W. A. Saunders, Ph. D. Dissertation, University of California, Berkeley, 1986; W. A. Saunders, K. Clemenger, W. A. de Heer, and W. D. Knight, Phys. Rev. B **32**, 1366 (1985).
- [37] H. A. Jahn and E. Teller, Proc. R. Soc. London Ser. A **161**, 220 (1937).
- [38] V. M. Strutinsky, Nucl. Phys. A **95**, 420 (1967); Nucl. Phys. A **122**, 1 (1968).
- [39] R. N. Barnett, C. Yannouleas, and U. Landman, Z. Phys. D **26**, 119 (1993).
- [40] (a) C. Yannouleas and U. Landman, Phys. Rev. B **51**, 1902 (1995); (b) J. Chem. Phys. **107**, 1032 (1997).
- [41] C. Yannouleas and U. Landman, Phys. Rev. Lett. **78**, 1424 (1997).
- [42] C. Yannouleas and U. Landman, J. Phys. Chem. A (Letter) **102**, 2505 (1998).
- [43] C. Yannouleas and U. Landman, J. Phys. Chem. (Letter) **99**, 14577 (1995); C. Yannouleas, R. N. Barnett, and U. Landman, Comments At. Mol. Phys. **31**, 445 (1995).
- [44] C. Yannouleas and U. Landman, J. Chem. Phys. **105**, 8734 (1996); Phys. Rev. B **54**, 7690 (1996).
- [45] C. Yannouleas and U. Landman, J. Phys. Chem. B (Letter) **101**, 5780 (1997); C. Yannouleas, E. N. Bogachek, and U. Landman, Phys. Rev. B **57**, 4872 (1998).
- [46] S. M. Reimann, M. Brack, and K. Hansen, Z. Phys. D **28**, 235 (1993).
- [47] S. Frauendorf and V. V. Pashkevich, Ann. der Physik **5**, 34 (1996).
- [48] H. Koizumi, S. Sugano, and Y. Ishii, Z. Phys. D **28**, 223 (1993); M. Nakamura, Y. Ishii, A. Tamura, and S. Sugano, Phys. Rev. A **42**, 2267 (1990).

- [49] A. Vieira and C. Fiolhais, Z. Phys. D **37**, 269 (1996).
- [50] W. Kohn and L. J. Sham, Phys. Rev. **140**, A1133 (1965).
- [51] M. L. Homer, E. C. Honea, J. L. Persson, and R. L. Whetten, (unpublished).
- [52] W. A. De Heer, Rev. Mod. Phys. **65**, 611 (1993).
- [53] J. Harris, Phys. Rev. B **31**, 1770 (1985).
- [54] W. M. C. Foulkes and R. Haydock, Phys. Rev. B **39**, 12 520 (1989).
- [55] M. W. Finnis, J. Phys.: Condens. Matter **2**, 331 (1990).
- [56] E. Zaremba, J. Phys.: Condens. Matter **2**, 2479 (1990).
- [57] The choice of the ETF energy functional as a vehicle for optimization of the input density is a rather natural one. Indeed, in several attempts (such as the integral formulation of density functional theory [W. Yang, Phys. Rev. A **38**, 5494 (1988)], or through the use of generalized nonlocal kinetic-energy functionals [L.-W. Wang and M. P. Teter, Phys. Rev. B **45**, 13 196 (1992)]) to construct theories based on the Hohenberg-Kohn density functional theorem [P. Hohenberg and W. Kohn, Phys. Rev. **136**, B684 (1964)] directly, that is without the use of orbitals, the ETF functional [see Wang *et al.* above] (with the kinetic functional expanded in density gradients), or the TF density [see, Yang above] appear as a limiting case, or lowest level of approximation, respectively.
- [58] Here we use the Gunnarsson-Lundqvist xc functional [see O. Gunnarsson and B. I. Lundqvist, Phys. Rev. B **13**, 4274 (1976)].
- [59] C. H. Hodges, Can. J. Phys. **51**, 1428 (1973).
- [60] M. Brack, Phys. Rev. B **39**, 3533 (1989).
- [61] Here, we consider clusters of monovalent elements (Na, K, Cu, etc.). For polyvalent elements, N in Eq. (18) must be replaced by Nv , where v is the valency.
- [62] For materials with high electronic densities, it is known that the usual LDA fails to provide adequate values for the surface tension. Therefore, in Ref. [40] (see also Ref. [28] for the case of fullerenes), in the case of Cu and Li clusters, we have carried an ETF calculation using the *stabilized-jellium*-LDA (SJ-LDA) functional, which yields substantially improved values for the surface tension. It is also well known that both the simple-jellium LDA and the stabilized-jellium LDA in the case of plane-surface calculations yield only approximate values for the Work Function. In our method, we can easily overcome these LDA discrepancies by taking the Work Function and the surface tension from experimental observations. This latter procedure has the additional advantage that contributions from the atomic d electrons in the case of noble-metal clusters (i.e., Ag, Au, Cu) are automatically included in the SE-SCM (see Refs. [41,42]).
- [63] I. S. Gradshteyn and I. M. Ryzhik, *Table of integrals, series, and products* (Academic, New York, 1980), ch. 8.11.
- [64] R. W. Hasse and W. D. Myers, *Geometrical relationships of macroscopic nuclear physics*, (Springer-Verlag, Berlin, 1980) ch. 6.5.
- [65] S. G. Nilsson, K. Danske Vidensk. Selsk. Mat.-Fys. Medd. **29** (1955), no. 16.
- [66] J. R. Nix, Annu. Rev. Nucl. Part. Sci. **22**, 65 (1972).
- [67] R. K. Bhaduri and C. K. Ross, Phys. Rev. Lett. **27**, 606 (1971).
- [68] The perturbation $I^2 - \langle I^2 \rangle_n$ in the hamiltonian (27) influences the shell correction $\Delta E_{\text{sh}}^{\text{Str}}$, but not the average, \bar{E}_{sp} , of the single-particle spectrum, since $U_0 = 0$ for all shells with an effective quantum number n higher than the minimum number required for accomodating N_e electrons (see, Ref. [1], p. 598 ff.).

- [69] J. Maruhn and W. Greiner, Z. Phys. **251**, 431 (1972).
- [70] M. G. Mustafa, U. Mosel, and H. W. Schmitt, Phys. Rev. C **7**, 1519 (1973).
- [71] This meaning of the variable ρ should not be confused with the meaning of ρ as a particle density in a density functional (see section II.A).
- [72] *Handbook of mathematical functions*, edited by M. Abramowitz and I. A. Stegun (Dover, New York, 1965).
- [73] B. K. Jennings, Nucl. Phys. A **207**, 538 (1973); B. K. Jennings, R. K. Bhadhuri, and M. Brack, Phys. Rev. Lett. **34**, 228 (1975).
- [74] A. Bulgac and C. Lewenkopf, Phys. Rev. Lett. **71**, 4130 (1993).
- [75] C. Br  chignac, Ph. Cahuzac, F. Carlier, M. de Frutos, and J. Leygnier, J. Chem. Phys. **93**, 7449 (1990).
- [76] C. Br  chignac, Ph. Cahuzac, J. Leygnier, and J. Weiner, J. Chem. Phys. **90**, 1492 (1989).
- [77] Z. Penzar and W. Ekardt, Z. Phys. D **17**, 69 (1990).
- [78] M. P. I  niguez, J. A. Alonso, M. A. Aller, and L. C. Balb  s, Phys. Rev. B **34**, 2152 (1986).
- [79] C. Br  chignac, Ph. Cahuzac, F. Carlier, J. Leygnier, and A. Sarfati, Phys. Rev. B **44**, 11 386 (1991).
- [80] For a detailed description of the BO-LSD-MD method, see R. N. Barnett and U. Landman, Phys. Rev. B **48**, 2081 (1993).
- [81] F. Garc  as, J. A. Alonso, M. Barranco, J. M. L  pez, A. Ma  anes, and J. N  meth, Z. Phys. D **31**, 275 (1994).
- [82] H. Koizumi and S. Sugano, Phys. Rev. A **51**, R886 (1995).
- [83] A. Rigo, F. Garc  as, J. A. Alonso, J. M. L  pez, M. Barranco, A. Ma  anes, and J. N  meth, Surf. Rev. and Letters **3**, 617 (1996).
- [84] The two-intersected-spheres jellium has also been used for describing the fusion of two neutral magic clusters (see Ref. [86]).
- [85] In this three-variables parametrization, the B parameter controls the necking-in, the C parameter controls the distance, and the α parameter controls the asymmetry, leaving no freedom for the shapes of the parent or the emerging fragments to be varied. In particular, both fragments remain simultaneously either prolatelike or oblatelike, while final spherical shapes are excluded altogether. The weaknesses of the "funny hills" parametrization with respect to metal-cluster fission have been discussed in Ref. [24].
- [86] O. Knospe, R. Schmidt, E. Engel, U. R. Schmitt, R. M. Dreizler, H. O. Lutz, Phys. Lett. A **183**, 332 (1993).
- [87] S. Wolf, G. Sommerer, S. Rutz, E. Schreiber, T. Leisner, L. W  ste, and R. S. Berry, Phys. Rev. Lett. **74**, 4177 (1995).
- [88] Notice that experimental measurements at $N = 33$ and 35 have not been obtained (see Ref. [36]).
- [89] I. Katakuse, T. Ichihara, Y. Fujita, T. Matsuo, T. Sakurai, and H. Matsuda, Int. J. Mass. Spectrom. Ion Processes **67**, 229 (1985).
- [90] M. M. Kappes, M. Sch  r, U. R  thlisberger, C. Yeretizian, and E. Schumacher, Chem. Phys. Lett. **143**, 251 (1988).